FUNCTIONAL NANOPLASMONIC DEVICES AND NOVEL PHOTONIC MATERIALS

A THESIS SUBMITTED TO

THE GRADUATE SCHOOL OF ENGINEERING AND SCIENCE

OF BILKENT UNIVERSITY

IN PARTIAL FULFILLMENT OF THE REQUIREMENTS FOR

THE DEGREE OF

MASTER OF SCIENCE

IN

ELECTRICAL AND ELECTRONICS ENGINEERING

By

Enes Battal

June, 2015

FUNCTIONAL NANOPLASMONIC DEVICES AND NOVEL PHOTONIC MATERIALS

By Enes Battal

June, 2015

We certify that we have read this thesis and that in our opinion it is fully adequate, in scope and in quality, as a thesis for the degree of Master of Science.

Assist. Prof. Dr. Ali Kemal Okyay (Advisor)

Assoc. Prof. Dr. Vakur Behçet Ertürk

Assoc. Prof. Dr. Hamza Kurt

Approved for the Graduate School of Engineering and Science:

Prof. Dr. Levent Onural

Director of the Graduate School

ABSTRACT

FUNCTIONAL NANOPLASMONIC DEVICES AND NOVEL PHOTONIC MATERIALS

Enes Battal

M.S. in Electrical and Electronics Engineering

Advisor: Assist. Prof. Dr. Ali Kemal Okyay

June, 2015

Plasmonics is one of the pillars of nanophotonics involving light matter interactions. Its applications found very wide range covering photovoltaics, photo-detection, optical communication, surface enhanced infrared absorption and Raman spectroscopy, infrared and THz imaging. Although the number of applications is very high, the underlying plasmonic structures are limited. In this thesis, we utilize a common plasmonic resonator structure namely metal-insulator-metal (MIM resonators) to realize active beam steering in the infrared spectrum. We investigate radiation characteristics of a phased array antenna formed by MIM resonators.

Materials-wise, low intrinsic loss, CMOS compatibility and bio-compatibility are among the crucial requirements for various applications of plasmonics. Noble metals are the dominant materials used in plasmonics to get high localization of the incident field among which gold and silver face serious challenges due to high intrinsic loss and lack of CMOS compatibility. We introduce InN as a novel plasmonic material thanks to its high concentration of free carriers and investigate its optical characteristics in the IR spectrum. We form a proof-of-concept absorber and investigate its plasmon excitation characteristics. On the other hand, we introduce another material ZnO, non-plasmonic, suitable for infrared imaging purposes with strong absorption characteristics.

Optical modulators are at the very heart of active light manipulation technologies such as integrated optics, bio-sensing, telecommunications, radio frequency and terahertz applications. Although various modulation schemes have been realized, the underlying mechanisms providing modulation did not change significantly. The common modulation methods can be listed as free carrier dispersion, thermo-optic method, use of liquid crystals, magneto-optical, optically nonlinear materials and recently introduced solid-state phase-change materials. Here we introduce another mechanism called resistive switching for optical modulation in the infrared spectrum. We investigate electrical resistive switching characteristics of an Al/ZnO/Si stack and optical modulation characteristics under electrical bias. We obtain hysteretic modulation in the reflection spectrum. We also investigate the thermo-optic modulation characteristics of atomic layer deposited ZnO through spectroscopic ellipsometry and realization of actively reconfigurable reflector surface.

Keywords: Electro-optic, thermo-optic, infrared, plasmonics.

ÖZET

İŞLEVSEL NANOPLAZMONİK AYGITLAR VE YENİ FOTONİK MALZEMELER

Enes Battal
Elektrik ve Elektronik Mühendisliği, Yüksek Lisans
Tez Danışmanı: Yrd. Doç Dr. Ali Kemal Okyay
Haziran, 2015

Plasmonik ışık ve madde arasındaki etkiletişimi inceleyen etkin nanofotonik alanlarından birisidir. Uygulama olarak güneş enerjısı, ışık detektörleri, optik iletişim, yüzey geliştirilmiş kızılötesi and Raman spektroskopi, kızılötesi and terahertz görüntüleme gibi alanları kapsamaktadır. Uygulama alanları çok olmasına ragmen plazmonik etkilerin gözlemlendiği yapılar limitlidir. Bu tezde, bilinen bir plazmonik yapı olan metal-yalıtkan-metal rezonatörlerin kızılötesi spektrumda aktif ışık yönlendirme uygulaması incelenecektir. Bu rezonatörlerle oluşturulan faz dizi anten konfigurasyonunun yayılma karakteristikleri incelenecektir.

Malzeme özellikleri açısından plazmonik uygulamalarda düşük iç kayıp CMOS fabrikasyon uyumluluğu ve biyo-uygunluk aranan kritik özellikler arasında gelmektedir. Plazmon uyarma malzemesi olarak asil metaller yüksek ışık lokalizasyonu için çok yaygın olarak kullanılmaktadır. Bunların arasından altın ve gümüş yüksek iç kayıp ve CMOS fabrikasyon uyumsuzluğu sorunlarını göstermektedir. Bu çalışmada yüksek sayıdaki serbest yük taşımasındasından olayı indiyum-nitratı CMOS fabrikasyonuna uygun kızılötesi plazmonik malzeme olarak incelenmektedir. Indiyum nitratın kızılötesi optik özellikleri, kızılötesi soğurucu uygulaması ve plazmon karakteristikleri incelenecektir. Diğer yandan, çinko-oksit alternatif plazmonik olmayan kızılötesi görüntüleme çalışmalarına uygun yüksek soğurucu özellikler gösteren malzeme olarak incelenecektir.

Optik modülatörler entegre optik, biyo-algılama, telekomunikasyon, radio frekansı ve terahertz uygulamaları gibi aktif ışık manipülasyon teknolojilerinin kalbinde bulunmaktadır. Bu uygulamalar için birden fazla optik modülasyon şemaları gerçekleştirilmiş olmasına ragmen altta yatan optik modülasyon mekanizmeleri çok değişmemiştir. En sık kullanılan modülasyon mekanizmaları arasında serbest yük kontrolü, termo-optik yöntem, sıvı kristal, opto-manyetik, lineer olmayan ve yeni ortaya çıkan katı katman faz değişimi malzemeleri yer almaktadır. Burada, direnç değişimi yöntemi yeni bir kızılötesi aktif modülasyon tekniği olarak sunulmaktadır. Al/ZnO/Si yığınının elektriksel direnç değişimi karakteristikleri ve elektrik uygulanması sırasında optik modülasyon karakteristikleri incelenmektedir. Işısal yansıma spektrumunda aktif histeresiz gösteren modülasyon gözlemlenmektedir. Bu çalışmanın yanı sıra, atomik katman kaplama tekniği ile büyütülmüş çinko-oksit malzemenin termo-optik modülasyön karakteristikleri de incelenmiştir. Bu malzeme spektroskopik elipsometre ile incelenmiş ve bununla aktif olarak değiştirilebilen yansıma yüzeyi tasarlanmıştır.

Anahtar Sözcükler: Elektro-optik, termo-optik, kızılötesi, plazmonik.

Acknowledgement

I am deeply grateful to Prof. Ali Kemal Okyay for his guidance and patience throughout my master's degree. He was my research advisor in not only my graduate years but also undergraduate years. He was an excellent supervisor and I am happy to be a member of his research team. I have learned a lot from him and always be grateful for everything he has done for me.

I would like to thank Prof. Vakur Ertürk and Prof. Hamza Kurt for being members of my thesis committee and making this thesis better with their valuable opinion.

I acknowledge TUBITAK (The Scientific and Technological Research Council of Turkey) for providing me a M.Sc. scholarship and funding research through TUBITAK-BIDEB. This work was supported by TUBITAK with grant numbers 109E044, 112M004, 112E052, 112M482, and 113M815.

I would like to thank our group members Fatih Bilge Atar, Feyza Bozkurt Oruç, Furkan Çimen, Yunus Emre Kesim, Ali Cahit Köşger Berk Berkan Turgut, Sami Bolat, Burak Tekcan, Ayse Özcan, Elif Özgöztaşı, Amin Nazirzadeh, Levent Aygün, Amir Ghobadi, Abdullah Gök, Seyma Canik, Gamze Ulusoy, Muhammed Maiz Ghauri Mehrab Ramzan and Sabri Alkış for making my graduate studies journey enjoyable.

Finally, my deepest gratitude goes to my family who have their signature at any success that I have achieved and will ever achieve throughout my entire life thanks to their endless love and support. I am extremely pleased to dedicate this thesis to *my family*.

Contents

List of Figures

List of Tables

Chapter 1

Introduction

1.1. Plasmonics

Plasmonics is the field investigating the light matter interactions at the sub-wavelength scale. When the light is incident on a surface with high amount of free carriers, charge polarization can be induced which can be transformed into oscillating charges associated with an electromagnetic wave bound to a surface called surface plasmon. Surface plasmons can provide immense light localization within a very small surface beyond the limits of conventional nanophotonics; therefore, enable the way to realize highly resonant optical devices.

Surface plasmons (SPs) have been tailored to improve the overall device performance in photovoltaics [1-3] and photo-detection [4-6] applications by realization of broadband or perfect absorbers. In bio-sensing, frequency selective resonant surface using SPs have been realized to introduce selectivity in biologic sample detection [7]. In addition, sensitivity enhancing plasmonic structures have been introduced for high performance bio-sensing [8]. In solid-state lighting, surfaces with enhanced scattering cross section have been achieved using metallic nanoparticles which utilize localized SPs [9, 10]. Metal-based plasmonic waveguides have been introduced in order to provide chip-to-chip optical communication in integrated optics applications [11, 12]. Optical modulators exploiting strong plasmonic resonators have been exploited to push the limits in modulation indices [13, 14]. Utilizing the localization properties of surface plasmons at sub-wavelength scales, nano-lithography below the diffraction limit has been realized in near-field lithography [15, 16]. The applications are not only limited to spectral region near the visible and infrared wavelengths. In the THz and microwave regions of the spectrum, ultra-broadband radar absorbers [17] as well as wave manipulators [18] have been realized. Depending on the application requirement, plasmonic structures with low-loss, high absorbing or high quality factor could be desired and their realization is highly dependent on the structure geometry as well as material properties. In this thesis, beam steering as a novel application of plasmonics is investigated; in addition, a new plasmonic material is introduced.

1.2. Optical modulation schemes

Optical modulators are at the very heart of active light manipulation technologies. Although the main push for advanced optical modulation technologies is due to overcome the interconnect bottleneck in current CMOS technology, recent efforts widened application range to bio-sensing [19], telecommunications [20], radio frequency and terahertz applications [21]. The demands for these applications can be listed as fast, high bandwidth, energy efficient, compact, scalable and integrable modulation technologies. To improve the manipulation abilities over the optical properties of matter, various number of modulation schemes utilizing resonant [22] or non-resonant [23] effects have been put forward. Yet, there is no significant change in the underlying mechanisms establishing optical modulation. The most common method of optical modulation is through field induced variation of free carriers within a semiconductor which would induce refractive index modulation [24]. Another method is thermo-optic modulation which is highly suitable for monolithic integration [25]; with additional cost of keeping thermal stability [20]. Among the alternatives, liquid crystals [26] are known to provide high refractive index variations, magneto-optical materials [27] allow fast switching, optically nonlinear materials [28] enable all optical modulation. However, these methods induce, additional fabrication costs due to their material-wise hybrid nature. A recently introduced method is solid-state phase-change [29] technique switching between metallic and dielectric phases via atomic scale modifications. This method offers large refractive index variation with fast switching speeds [30], low switching power [31] and provides non-volatility [30]. The research for enhancing the modulation performance along with aim for the low-cost and integration suitability continues. In this thesis, atomic layer deposited ZnO will be investigated as an alternative high performance dielectric material and a novel electro-optic modulation mechanism called resistive switching will be introduced.

1.3. Thesis Overview

In most of the work of this thesis, theoretical calculations based on finite difference time domain simulations and extraction of optical constants of dielectric materials via spectroscopic ellipsometry method is performed. Therefore, these methods will be described in Chapter 2 of this thesis in detail.

In Chapter 3, beam steering is introduced as a novel application of a plasmonic resonator called metal insulator metal (MIM). Radiation characteristics of a phased array antenna formed using MIM unit cells is investigated.

In Chapter 4, a new plasmonic material, InN, is introduced for infrared applications. Infrared optical characteristics of InN films are investigated and compared with Au. For proof-of-concept demonstration, a plasmonic infrared absorber is realized.

Chapter 5 presents the optical characterization of atomic layer deposited ZnO for infrared imaging applications. For various deposition temperatures, ZnO films are characterized through spectroscopic ellipsometry and a reference device based on this material is investigated and compared with commercially available counterparts.

In Chapter 6, atomic layer deposited ZnO is investigated as an alternative thermo-optic modulation material. Thermo-optic coefficients larger than conventional large band-gap materials have been obtained and a thin film thermally tunable reflective surface have been realized.

Lastly, in Chapter 7, a novel mechanism electro-optic modulation mechanism called resistive switching is introduced and investigated in depth. Electrical and opto-electronic characterization of Al/ZnO/Si resistive switching device is performed and theoretical calculation of refractive index modulation by taking the variation in te effective doping concentrations due to modification of local stoichiometry in the dielectric layer is performed.

Chapter 2

Methods

2.1. Finite difference time domain (FDTD) method

Finite difference time domain method is a simulation method developed for solving Maxwell`s time dependent curl equations (Eqs. 2.1 and 2.2).

$$\nabla \times E = -\frac{\partial B}{\partial t} \tag{2.1}$$

$$\nabla \times H = \sigma E + \frac{\partial D}{\partial t} \tag{2.2}$$

As the name implies, the solution is in time domain and performed by sending a short light pulse involving the range of desired frequencies. Eqs 2.1 and 2.2 are discretized using central difference approximation according to Yee`s FDTD algorithm[32]. In this thesis, a commercial Maxwell FDTD solver named FDTD solutions by Lumerical Inc is used. An exemplary simulation environment is shown in Figure 2.1. In the example, the simulations is bounded with perfectly matched layers (PML) in the +/- y directions to simulate infinite space and periodic boundary is assumed in the +/- x directions to have infinite repetition. The source injects the multi frequency plane-wave light from the top and the monitors collect the transmitted light through themselves to be Fourier transformed at the end of the simulation to get the steady state response of the structure.

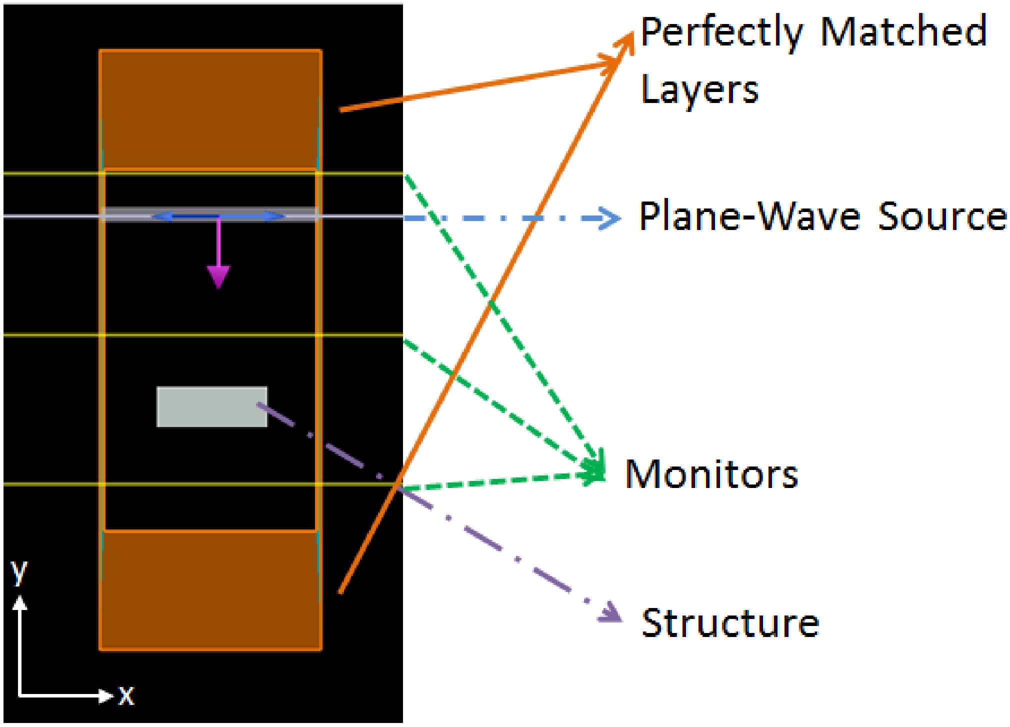

Figure 2.1 – An exemplary simulation environment

2.2. Spectroscopic ellipsometry

Any dielectric material can be optically defined by its complex refractive index, $\tilde{n} = n + jk$, which is the square root of its dielectric permittivity ε. Any material that propagates through a dielectric medium goes into polarization change. Spectroscopic ellipsometry method uses this change in the polarization upon reflection or transmission of incident light to extract the refractive index of the given material. In fact, more information such as film thickness, surface roughness, material composition, carrier concentration, band structure and mechanical properties can be extracted through theoretical modeling of the extracted data from the spectroscopic ellipsometry method. In this thesis, spectroscopic reflection ellipsometry is utilized to extract various properties of thin films.

A reflected light would undergo polarization change which is described by complex reflectance ratio

$$\rho = \tan(\Psi)\, e^{j\Delta} = \frac{r_p}{r_s} \tag{2}$$

experimentally extracted by measuring Ψ and Δ which are amplitude ratio and phase shift. In order to measure these parameters, the incident light is passed through a polarizer to fix the initial polarization to a known state. Then the polarization of the reflected light is measured by passing through a polarization matching device set called compensator and analyzer. In order to match to the polarization of the reflected light the compensator and analyzer rotate which result in a changing intensity at the detector. This intensity is maximized when the matching to the polarization of the reflected light is accurate. A depiction for this configuration is shown in Figure 2.2.

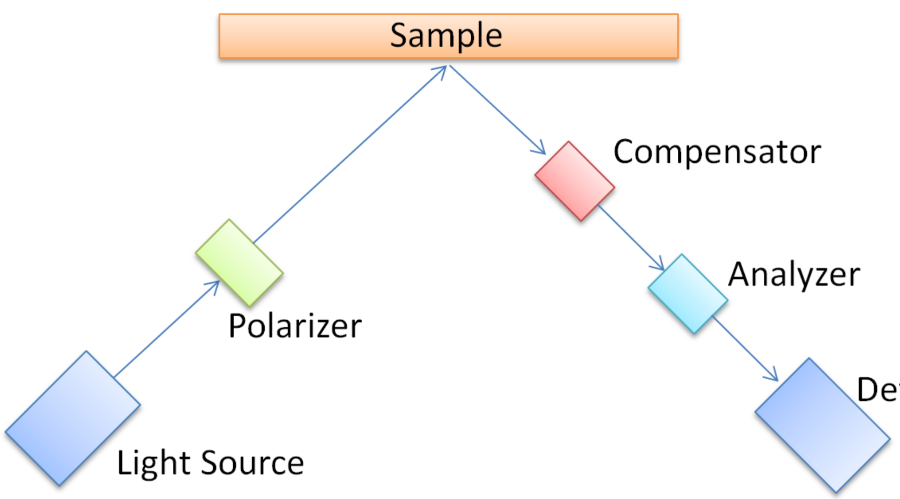

Figure 2.2 – Depiction of a rotation compensator-analyzer spectroscopic ellipsometers device.

When the measurement is complete, Ψ/Δ pair is converted to Fresnel reflection coefficients and fit using oscillator functions modeling the dielectric permittivity such as Lorentz, Drude, Cody-Lorentz and Gaussian oscillators to determine the refractive index.

In this thesis the spectroscopic ellipsometry measurements are performed using commercial ellipsometers V-Vase and IR-Vase by J. A. Woollam Co. for UV- VIS-NIR and Mid-IR wavelengths, respectively.

Chapter 3

Metal insulator metal plasmonic infrared beam steering

This chapter is based in part on the publication "Metal-dielectric-metal plasmonic resonators for active beam steering in the infrared," **E. Battal**, and A. K. Okyay, Optics Letters Vol. 38, Issue 6, pp.983-985 (2013). Reproduced (or 'Reproduced in part') with permission from Optical Society of America Publishing Group. Copyright 2013 Optical Society of America

3.1 Introduction

Previously, a vast amount of research effort is spent on steering the light beams. Holographic imaging technologies [33] and novel optical communication schemes [34] highly depend on controlling the propagation of light in active fashion. Such purposes lead the researchers to investigate reconfigurable diffraction gratings [35], movable micro lens arrays [36], tunable waveguides [37], electro-optic prisms [38], and leaky wave antennas [39]. The dominant technique to achieve non-mechanical beam steering is active modulation of refractive index. Magneto-optic [40], nonlinear [41], phase change [42] materials, doped semiconductors [43] and liquid crystals [35] are among the most commonly used materials for refractive index control. Novel beam steering devices utilizing surface plasmons (SPs) appeared at operation frequencies of near [44] and mid [45] infrared wavelengths.

In the literature, metal-insulator-metal (MIM) devices are used to achieve strong plasmon resonances [46]. Within these devices, surface plasmons propagate at the metal insulator interfaces in a coupled fashion resulting in very high localizations within very small volumes. The optical properties of such devices are shown to be manipulated using refractive index modulation [46]. With such a property, one can utilize these devices for the purpose of beam steering.

In this chapter of the thesis, a phased array configuration of MIM plasmonic resonators operating at mid-infrared wavelengths is formed to realize beam steering. The radiation pattern of the phased array is investigated to extract the beam steering characteristics.

3.2. Device structure and simulation setup

The investigated structure is made of MIM resonators depicted in Figure 3.1. Due to computational limitations a phased array formed by five individual MIM resonators is investigated in this work. Each MIM resonator is formed by a dielectric layer placed in between two metallic layers. The device is assumed to be semi-infinite in z-direction described in Figure 3.1. To simplify the analysis, dielectric (t_d) and metal (t_m) thicknesses are taken as 300nm and 100nm, respectively, and the center to center distance (d) between each MIM resonator is chosen as 2300nm. FDTD method is performed to analyze the radiation pattern of the structure. A plane-wave like illumination provided by the total field scattered field source is used to have in phase excitation of each array element. The illumination is from the top of the structure with a linear polarization having electric field vector along x-axis to achieve surface plasmon excitation and the wavelength λ is chosen as 10 µm. Perfectly matched layers boundary condition is assumed in all directions. A near field to far-field projection technique is utilized to extract the far field radiation pattern at about 1m which is much higher than the device dimensions. The dielectric constants for the metal sections of the device are chosen to be of gold (Au), and the device is assumed to be suspended in air. The dielectric layer whose refractive index is to be modulated is chosen as Silicon. A widely used optical constants provided by Palik [47] are used in the simulations. The refractive index of Si is decreasing from 3.42 to 3.27 as the carrier concentration of Si is reaches to the order of 10^{18} cm^{-3} from intrinsic values. The extinction coefficient of Si (k_{Si}) is neglected since it is below 0.032 [47] where such an assumption wouldn`t produce change in the radiation pattern. Since modulation of electron concentration within Si can be achieved by several means such as thermal [48], electrical [43] or optical [49], the device is expected to be of practical use.

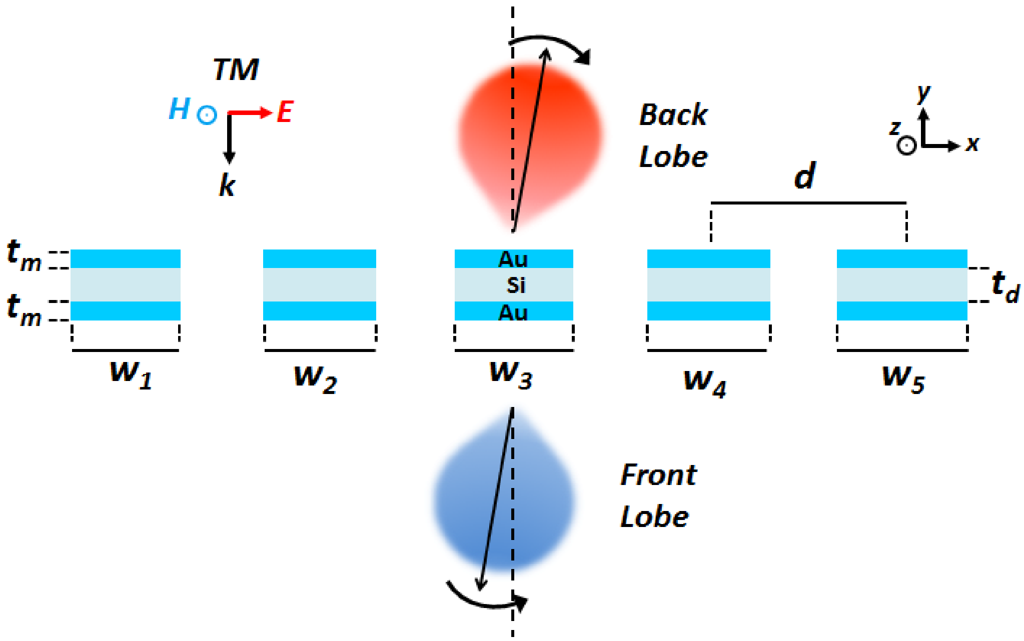

Figure 3.1 – The phased array antenna like configuration of MIM resonators having different width values. Copyright 2013 Optical Society of America

3.3 Results and discussion

3.3.1 Radiation characteristics of a single resonator

Surface plasmon Fabry-Perot (SP-FP) resonances can be realized within a finite plasmonic cavity formed by the top and bottom metal dielectric interfaces of an MIM device. A clear depiction is provided in Figure 3.2a such that constructive interference of right propagating SPs (R-SP) and the left propagating SPs (L-SP) occurs [46]. The resonance can be described by the formula

$$k_0 n_{eff} w = m\pi + \varphi \qquad (5.1)$$

where k_0 is the wave-vector of the incident light, n_{eff} is the effective refractive index inside waveguide, w is the width of the slab, m is an integer and φ is the phase picked up by SPs upon reflection at the ends of the waveguide. The dispersion relation of MIM waveguide [46] gives, n_{eff}, as 3.72 for the wavelength of $\lambda = 10$ µm.

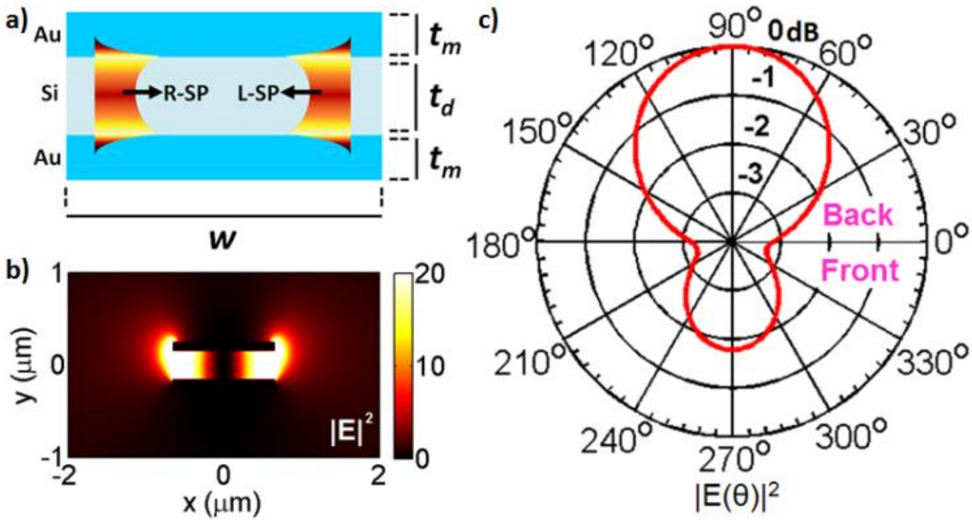

Figure 3.2 - (a) MIM resonator unit having right (R-SP) and left (L-SP) propagating SPs. b) A standing wave is formed within the MIM cavity due to Fabry-Perot resonance. c) Radiation pattern of an MIM resonator unit resembling similarity to that of a dipole except with the asymmetry in the front and back intensities. Copyright 2013 Optical Society of America

Initially, the radiation characteristics of an MIM resonator unit depicted in Figure 3.2a is studied. The first order resonance condition (m=1) satisfying Eq. (5.1) requires the width of the MIM resonator, w, to be 1320nm at $\lambda = 10$ µm. For the given condition, very high localization is achieved within the MIM cavity as depicted in Figure 3.2b. Such localization is due to the excited SP-FP mode. The resulting radiation pattern is similar to that of a dipole; however, there is a slight asymmetry due to having excitation from the top. Front and back lobe directivities are extracted to be 0.053 dBi and 1.83 dBi, respectively. Half power beam widths (HPBW) of the front and back lobes are both higher than 150^o. As the overall structure is symmetric about y-axis, the resulting lobes are also symmetric at around y-axis.

3.3.2 Phased array antenna characteristics

To achieve beam steering with a phased array antenna, each element of the array is fed with a different phase. In phased array MIM structure, the phase shift is achieved by modulation of refractive index for each element. An important point is that the widths of each unit should be different to achieve different phase shifts for each unit when the refractive indices of MIM resonators are modified collectively. Therefore, the widths of five MIM resonator units, w_1, w_2, w_3, w_4 and w_5 are selected as 1320, 1380, 1440, 1500 and 1560 nm, respectively. These values are reached as a result of a parameter sweep around the resonant value (1320 nm). The resulting radiation pattern of the phased array device is shown in Figure 3.3a. At the refractive index value for intrinsic Si (n_{Si} = 3.42), the front and back lobes of the array MIM structure are deflected by -4.7^o and -8.3^o, respectively, as a result of different phase shift contributions from each element. Directivity values surpass the previous value by increasing to 3.96 dBi for the front lobe and to 7.11 dBi for the back lobe. A significant decrease in the HPBW of the front and back lobes from the previous values to 42^o and 42.6^o, respectively. These improvements are as a result of the array factor which would be introduced in the radiation pattern formulation.

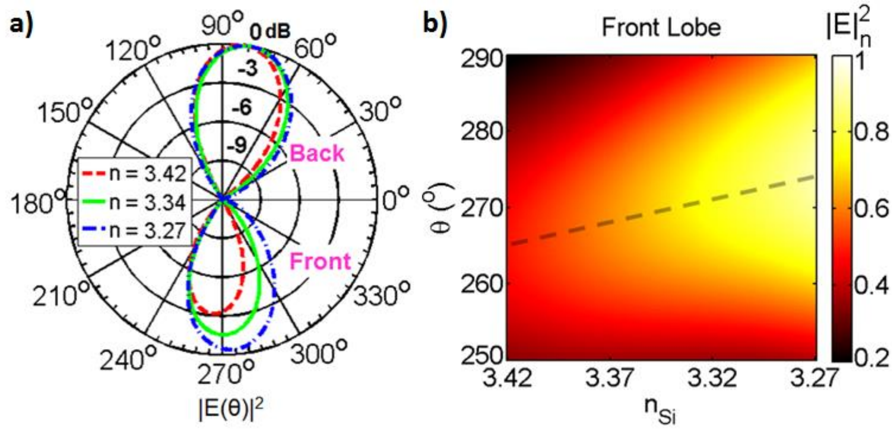

Figure 3.3 - (a) The front lobe of the phased array-like MIM structure shifts by 8.75° and the back lobe shifts by 2.35° when n_{Si} changes by 0.15. b) Normalized radiation intensity ($|E|^2_n$) at the center of the front lobe shifts continuously and its amplitude increases by decreasing n_{Si}. Copyright 2013 Optical Society of America

Figure 3.3a depicts the achieved active beam steering by refractive index modulation. While changing n_{Si} from 3.42 to 3.27, the front lobe steers by 8.75° from 265.25° to 274°. A continous sweep of n_{Si} results in a continuous beam steering as shown in Figure 3.3b. The back lobe exhibits poor steering characteristics with a value of 2.35°. Only a slight change in the HPBW of the front lobe (3.4°) is observed due to the modulation of refractive index.

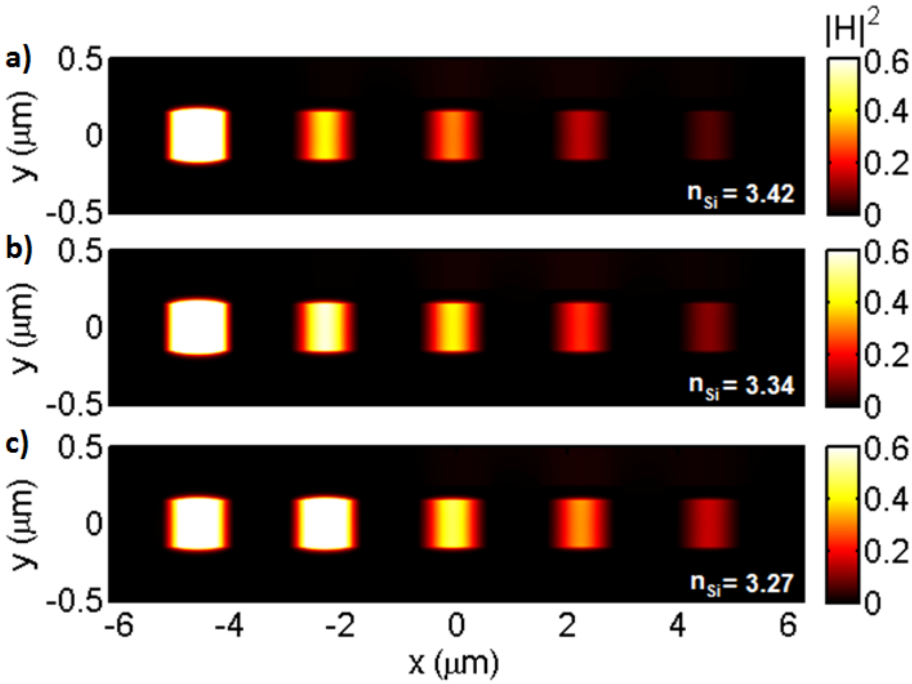

Figure 3.4 - Magnetic field intensity ($|H|^2$) profile indicates a shift of resonant behavior towards wider elements (to right) as n_{Si} decreases intermittently from (a) 3.42, to (b) 3.34 and (c) 3.27. Copyright 2013 Optical Society of America

Extraction of H field intensity profiles shows the phased array like behaviour in Figure 3.4. From Figure 3.4a to 3.4c, the resonance strength of each resonator unit changes with the decreasing refractive index value and the resonance strength for each element is always different for each case indicating introduction of different phase shifts for the radiated field from these cavities.

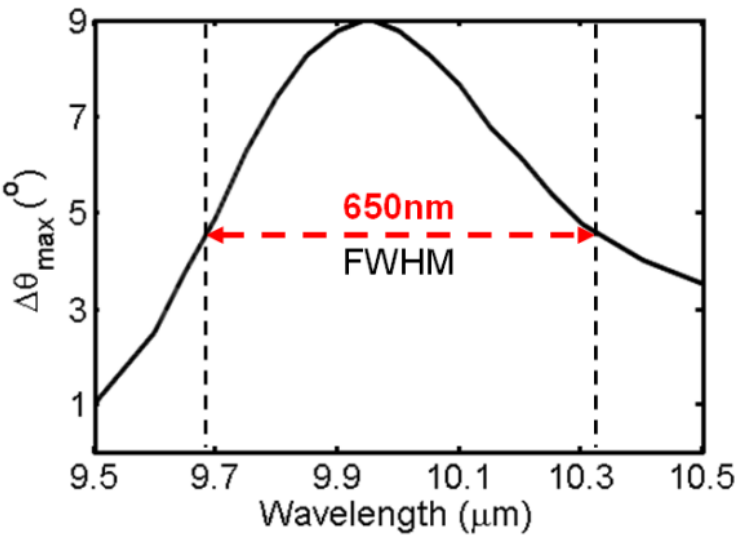

Figure 3.5 - Maximum beam steering angle, $\Delta\theta_{max}$, is relatively preserved within a full-width half-maximum of 650nm around the operation wavelength (λ = 10 μm). Copyright 2013 Optical Society of America

Keeping the refractive index of Si the same, the beam steering ($\Delta\theta_{max}$) for the front lobe remains the same within a spectral full width half maximum (FWHM) of 650nm between 9.68 – 10.33 μm wavelength range as depicted in Figure 3.5. This spectrum is highly beneficial for introducing beam steering to commercial CO_2 lasers [50].

3.4. Conclusion

In this section of this thesis, beam steering is achieved utilizing metal-insulator-metal resonators within a phased array antenna configuration at infrared operation frequencies. A continuous-angle beam steering of 8.75^o is calculated as a result of modulation of refractive index of Si by 0.15. A spectral steering bandwidth of 650-nm- is achieved for the 10μm center wavelength. The beam steering is observed to introduce no modification in the divergence angle of the device. The phased array antenna concept formed by MIM resonators demonstrated here can be scaled to visible frequencies as well as THz frequencies.

Chapter 4

InN based infrared plasmonics

4.1. Introduction

Plasmonics found very wide range of applications covering photovoltaics [51], photo-detection [6], bio-sensing [52], optical communications [53], surface enhanced infrared absorption (SEIRA) [54] and Raman spectroscopy [55], infrared and THz imaging [56]. Most desired material properties for these applications of plasmonics are low intrinsic loss, CMOS compatibility and bio-compatibility. Noble metals have been the dominant material for surface plasmon excitation to get high localization of the incident field. Out of noble metals, gold and silver are considered problematic due to lack of CMOS compatibility and their relatively high loss. For various applications, large negative real part of the permittivity is also desired. To satisfy these needs, look for new plasmonic material has begun recently. Semiconductors with high amount of free carriers such as Al:ZnO [57], ITO [58], TiN [59] have been considered as good alternatives fulfilling the necessities. Alternatively, InN with metallic In [60] islands have attracted attention for the applications within the terahertz spectrum [61]. Yet, this material is not investigated for applications in infrared spectrum although its high concentration of electrons makes it viable.

In this chapter of the thesis, optical properties of high-pressure chemical vapor deposition (HPCVD) grown InN films are investigated for plasmonic application purposes in the mid-infrared spectrum. An infrared absorber surface with InN is realized for proof-of-concept demonstration. In the 3-20μm spectrum, spectroscopic ellipsometry technique is utilized to extract the optical constants of InN and its surface plasmon propagation characteristics are compared with that of Au. Strong plasmonic resonances are obtained by forming corrugated surfaces on an InN film and near perfect absorption is attained around 14μm wavelength.

4.2. Sample preparation

InN film is deposited on top of GaN/sapphire template. Corresponding scanning electron micrograph is depicted in Figure 4.1a. The InN film shows precipitated regions and 3D structures; however, the film can be assumed continuous with a certain surface roughness using effective medium theory. The device formation is realized on InN films by patterning via FEI Nova 600i NanoLab focused ion beam device using Ga^+ ions accelerated under 30kV potential with 96pA current. Within 100 x 50 μm^2 area corrugations are formed on top of InN films as depicted in Figure 4.1b. The structural parameters of the corrugations such as depth, width and the period of the gratings are varied between, 300-900nm, 2-5μm, 5-10μm, respectively**,** to observe the effect of grating parameters on the plasmonic response. Strong charge polarization can be observed with large penetration of the incident field to the corrugations; therefore, the etching depth is kept at least at 300nm.

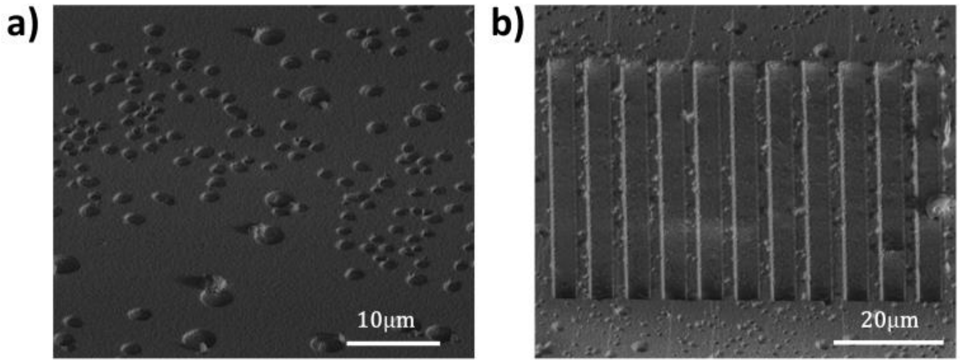

Figure 4.1 – Scanning electron microscopy images of a) as grown HPCVD InN films and b) corrugated plasmonic structures

4.3. Optical characterization

At angle of incidences of 40° and 55°, spectroscopic ellipsometry measurements are carried out in order to obtain the optical properties of the InN films. Then, accurate modeling of dielectric constant, ε, is performed through spectral fitting of Drude and Lorentz oscillators which would include the effects of optical phonon modes and free carriers as well. The corresponding formulation is :

$$\varepsilon(E) = \varepsilon_{\infty} - A_D \frac{\Gamma_D}{E^2 - j\Gamma_D E} + A_L \Gamma_L \frac{E_o^2}{E_o^2 - E^2 - j\Gamma_L E} \qquad (8.1)$$

where ε_{∞} is the static dielectric permittivity, E is the photon energy, E_o is the center frequency of the Lorentz oscillator, A and Γ are the oscillator amplitude and broadening, respectively for the Drude and Lorentz oscillators denoted by D and L in the subscript, respectively. For the as-grown films, 3.33, 11.42, 81.4, $3.16\text{x}10^{-2}$ eV, $6.28\text{x}10^{-3}$ eV, $5.89\text{x}10^{-2}$ eV, are the values found to best fit ε_{∞}, A_D, A_L, Γ_D, Γ_L and E_o parameters, respectively. The fittings resulted a film thickness of about 950nm. For the Drude oscillator, the relations A = $(\hbar\mu eN)/(\varepsilon_o m^*)$ and B = $(\hbar e)/(\mu m^*)$, where ħ is the Planck's constant, e is the unit electronic charge, ε_o is the free space permittivity, m^* is effective mass of electrons, μ is the electron mobility, N is the carrier concentration, give the mobility and carrier concentration of InN films as $2.88\text{x}10^{19}$ cm^{-3} and 332.6 cm^2/V.s, respectively with $m^*=0.11m_o$ [62]. The extracted carrier mobility is in the range of reported values for InN [63]. Figure 4.2a and 4.2b show the obtained dielectric permittivity values along with that of Au [64] for comparison purposes. The dielectric constant of InN is lower than that of Au because of the higher plasma wavelength which is about 3.76μm compared to Au for which it is in the visible spectrum. The film exhibits phonon-modes centered at 21.05μm, which effects the dielectric permittivity significantly. The observed phonon mode is identified as E_1^{TO} [65]. Plasmonic characteristics of InN films have been investigated through extraction of propagation length (L_P) and mode size (D_W) which indicates field confinement and compare these values with that of Au using the following relations,

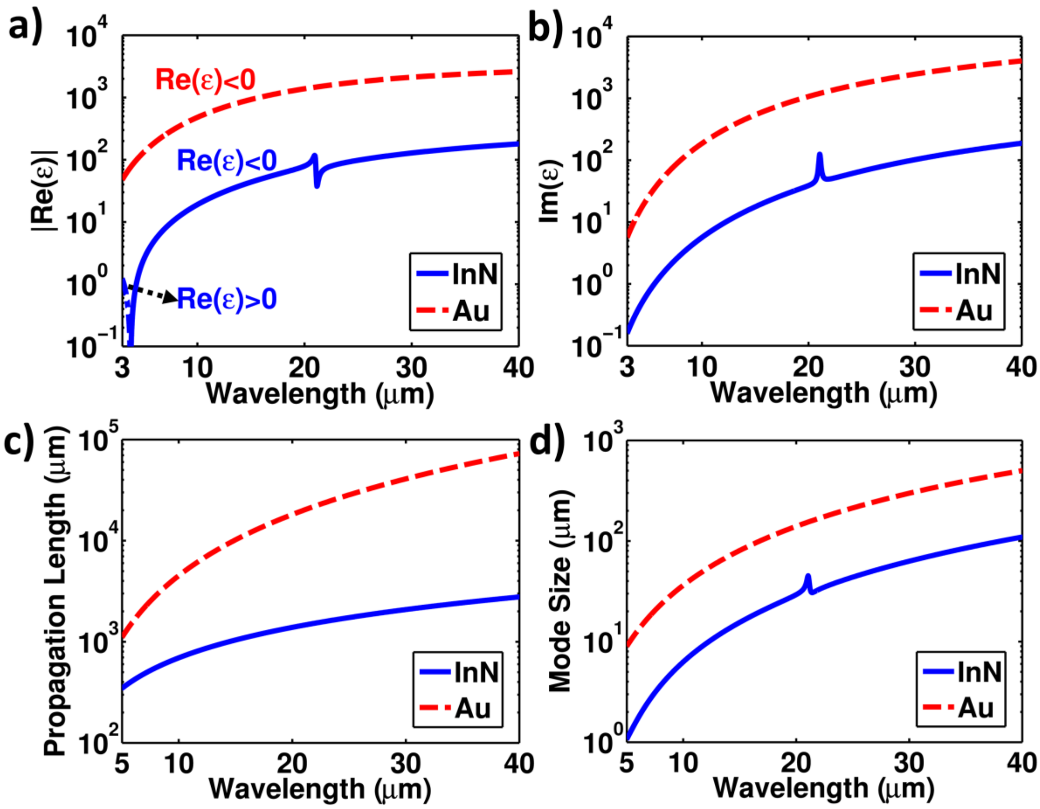

Figure 4.2 – Comparison of optical properties of Au and InN for a) real and b) imaginary parts of their dielectric permittivity, c) plasmon propagation length and d) mode size assuming they contact with air interface.

$$L_P = 1/\,\mathrm{Im}\left(k_0\sqrt{\frac{\varepsilon_m}{\varepsilon_m+1}}\right) \tag{8.2}$$

$$D_W = \begin{cases} \delta_{air} & |\varepsilon_m| \geq e \\ \delta_{air} + \delta_m \ln \dfrac{e}{\varepsilon_m} & |\varepsilon_m| \geq e \end{cases} \quad (8.3)$$

where $\delta_{air} = 1/\mathrm{Re}\left(k_0\sqrt{-1/(\varepsilon_m+1)}\right)$, $\delta_m = 1/\mathrm{Re}\left(k_0\sqrt{-\varepsilon_m{}^2/(\varepsilon_m+1)}\right)$, and k_0 is the free space wave-vector and ε_m is the dielectric permittivity of the plasmonic material. Figure 4.2c depicts surface plasmon propagation length along Au/air interface which exceeds that of InN/air interface by one order of magnitude; whereas InN offers better mode confinement as depicted in Figure 4.2d. These properties make InN as a good candidate for plasmonic filter/absorber structure design.

4.4. Device analysis

A representative depiction of the single dimensional plasmonic grooves patterned on fresh InN films is depicted in Figure 4.3a. In order to verify the extracted optical constants, fourier transform infrared (FTIR) reflection measurements from the fresh InN films at normal incidence is performed using Bruker Vertex 70 FTIR Spectrometer with Hyperion Microscope attachment. The reflection spectra are compared with simulation results assuming a flat 950-nm-thick InN film FDTD method. Throughout 3-20µm spectrum a very good agreement between experimental and theoretical results is achieved and depicted in Figure 4.3b. Slight disagreement at the higher wavelengths and lower wavelengths is attributed to the surface roughness of the films. In the un-patterned film optical Fabry Perot resonance is observed for the quarter-wave film thickness corresponding to the wavelength of 3µm in agreement with the formulation $d = m\lambda/4n$ for m=1 where d is the thickness of the film, m is the order of the resonance, n is the refractive index of the film. As a result of this resonance, strong absorption is observed around the wavelength of resonance.

The excitation of surface plasmons is highly dependent on having charge polarization along a metal-dielectric interface. For the corrugations formed by InN, the incident light should have electric field component perpendicular to the corrugations (transverse magnetic, TM, polarization) for this purpose. In order to observe surface plasmon resonance on InN films, the gratings width and period is selected to be 6μm and 10μm, respectively and the corresponding reflection spectra is depicted in Figure 4.3c. The strength of the resonance can be measured from the strength of the absorption which is highest at around 14μm. FDTD simulations of the patterned structure is

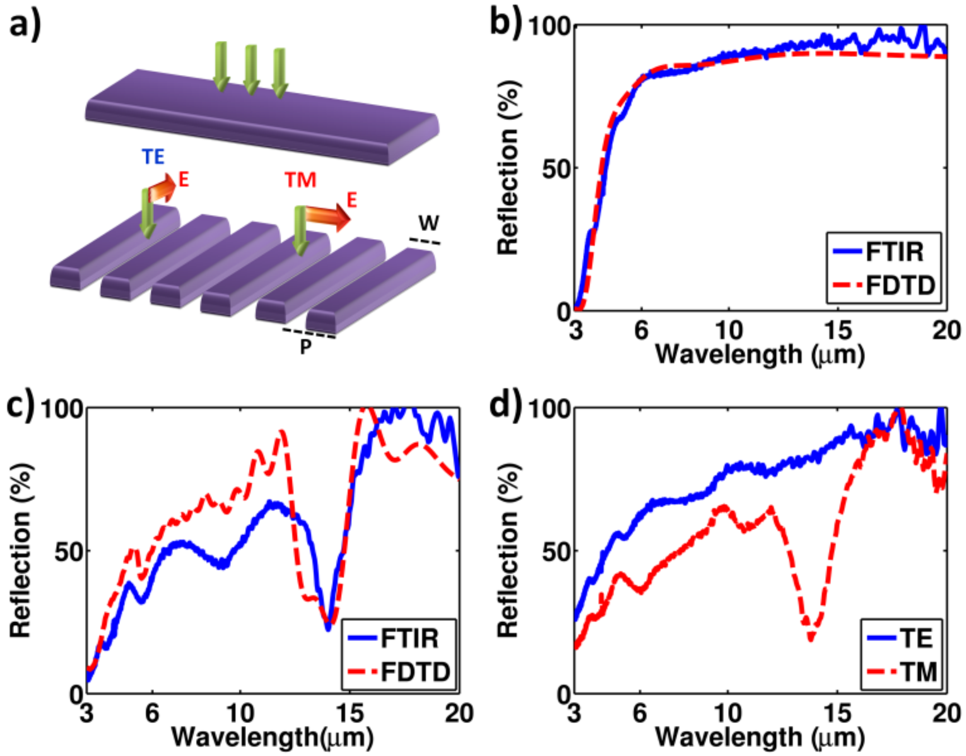

Figure 4.3 – Device structure with reflection characteristics. a) Representative image for fresh and corrugated films. b) FTIR reflection spectra of the un-patterned film agrees well with FDTD simulations c) The patterned grating structure with the period (P) of 10μm and width (W) of 6μm shows surface plasmon assisted strong absorption at around 14μm. d) The structure exhibits plasmon resonance in TM polarization and no- plasmonic resonance at TE polarization as expected.

performed assuming InN gratings on top of 800nm GaN and c-plane sapphire substrate.

In-plane optical constants of GaN [66] and c-Sapphire [67] existing in the literature are used. At the wavelength of strong resonances, the FDTD simulations and FTIR measurements agree very well in Figure 4.3c. The observed disagreements are attributed to the imperfections of the InN film which could reflect as higher modes of resonances or resonance broadening. The corrugated films exhibit polarization dependent reflection spectra which has a highly resonant plasmonic absorption at TM spectra and no plasmonic resonance for the TE spectra as expected. Reflection spectra for the flat film and corrugated film for TE polarization is similar with a slight difference of magnitude due to loss of light to the transmission spectrum as a result of light passing through the corrugations.

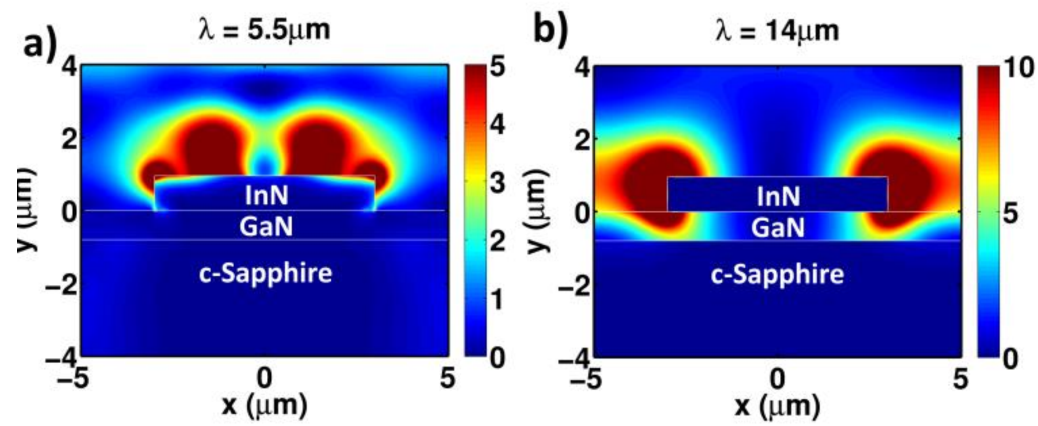

Figure 4.4 – Electric field intensity profiles for W=6μm, P=10μm, at the resonant wavelengths of a) λ = 5.5μm and b) 14μm.

In order to investigate the excited plasmon modes within the corrugated films, the electric field intensity profiles are extracted in Figure 4.4a and b. At λ = 5.5μm, the corrugated structure exhibits localized surface plasmon resonances around the film corners which in turn would enhance backward scattering and absorption. Moreover, the films exhibit strong excitation of propagating surface plasmons on top of InN/air interface. The excited SP resonance consists of two propagating waves reflected from the edges of the surface with π/2 phase shift. As a result, a constructive interference occurs and SP Fabry-Perot resonance arise. The constructive interference equation is given by $m=2n_{SP}W/\lambda+1/2$ where $n_{SP}=(\varepsilon_m\varepsilon_d/(\varepsilon_m+\varepsilon_d))^{1/2}$ is the effective refractive index for the SP, ε_d is the dielectric permittivity of the dielectric and m is an integer representing mode order. Since the dielectric layer is air, ε_d is 1, the order of mode is m=3. The arising resonances are not coupled such that there is no interaction between individual slabs of gratings. However, for the wavelength of 14μm in Figure 4.4b, there is strong periodic coupling between unit-cells arising from dipolar resonance excitations. The excited surface plasmon mode can be explained by the grating momentum matching formula $m2\pi/P = 2\pi n_{SP}/\lambda$ which matches the momentum obtained by the scattering due to gratings to that of surface plasmons. For this mode, effective index approximation is carried out since the resonant field interacts with both air and GaN layers. From the field profile it is apparent that most of the field is localized to the 2-μm-thick air region and 0.8-μm-thick GaN film; therefore, ε_d is found to be 1.43 assuming 2:0.8 air/GaN ratio satisfying the momentum matching of the first order SP mode (m=1).

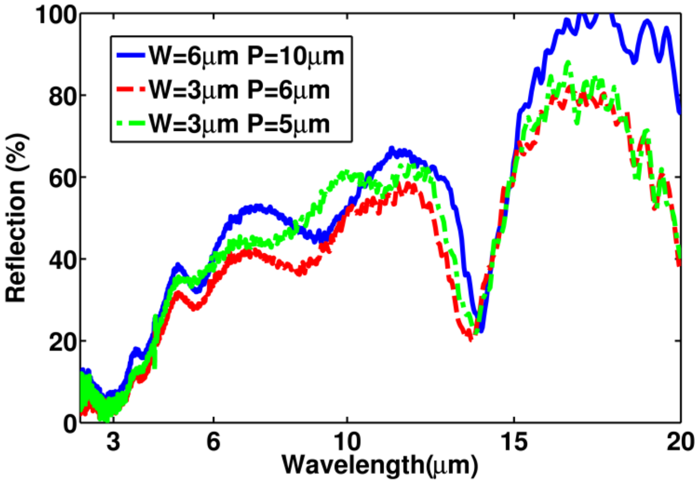

Figure 4.5 – Reflection spectra for different structure parameters under TM polarized light indicate that the resonant wavelengths of the plasmon modes red-shift with the increasing structure parameters.

The effect of structural parameters, W and P, on the plasmon resonances is explored in Figure 4.5. The location of the surface plasmon resonances do not shift with the decreasing width of the films significantly as a result of the decreased mode order around the same wavelengths. Decrease in the periodicity cause small red-shift of the resonances around 13.9μm to 13.8μmp; whereas, it is slightly higher for the resonance at 8μm.

4.5. Conclusion

HPCVD grown InN is introduced as an alternative plasmonic material for infrared applications. Optical properties of the InN films are investigated through spectroscopic ellipsometry technique within 3-20μm spectrum and observed that InN exhibits plasmon wavelength below the mid-IR range making it good alternative for plasmonics applications in the mid-IR range. Plasmon propagation loss and mode confinement characteristics of InN is compared with that of Au and found out that InN is better at mode confinement. A strong plasmonic absorber surface supporting more than one resonant plasmon modes including surface plasmon fabry perot mode and localized surface plasmon modes is realized. This study demonstrated the viability of InN as a plasmonic material which makes it suitable for bio-sensing and CMOS compatible plasmonic applications.

Chapter 5

Optical characterization of atomic layer deposited ZnO as a novel bolometric material

This chapter is based in part on the publication "Atomic-layer-deposited zinc oxide as tunable uncooled infrared microbolometer material," **E. Battal**, S. Bolat, M.Y. Tanrikulu, A. K. Okyay and T. Akin, Physica Status Solidi (a) applications and materials science Vol. 211, Issue 11, pp.2475-2482 (2014). Reproduced (or 'Reproduced in part') with permission from John Wiley and Sons Publishing Group. Copyright 2014 John Wiley and Sons

5.1. Introduction

Superior electronic and optical characteristics of ZnO [68, 69] made it find place within thin film electronics, sensors, and optoelectronics applications. Its high electron mobility allowed to realize thin film transistors as an alternative to amorphous Silicon [70, 71]. Due to large band-gap of ZnO, 3.37eV, large amount of self-doping induced by defects, ZnO has been widely used as a transparent conducting oxide [72, 73] in addition to an ultraviolet sensor [74]. However, its optical properties within the infrared (IR) region of the spectrum are not yet fully explored. One candidate application could be infared imaging where microbolometers are dominant. These devices can operate at room temperature and low cost, compact, CMOS compatible which make them preferable over other technologies. Similar to all other type of detectors, operation of a microbolometer depends on the absorption within an infrared sensitive layer. In general, this layer is also used as a structural layer to form the whole pixel. Most commonly employed material for this purpose is Si_3N_4 [75]. Currently, a vast amount of research effort is being made to increase the performance of the present microbolometers. One way of achieving this aim is to have materials with better absorption performance within the spectrum of interest.

For the case of ZnO, research on its infrared optical properties which is very crucial for infrared imaging applications, is very limited. Generally, free carrier effects and optical phonon modes are the dominant factors defining the dielectric constant of materials within the IR spectrum. Previously, it has been shown that pulsed laser deposited ZnO films have phonon modes within 300-600 cm^{-1} (~16μm-33μm) spectrum [76]. On the other hand, it has been known that atomic layer deposited (ALD) ZnO films have large amount of free carriers whose amount can be controlled via deposition parameters [77]; thus, it is expected to have free carrier dominant optical properties for ALD grown ZnO films. ALD grown ZnO is not yet explored as an infrared absorber layer for the microbolometer application purposes.

In this chapter of the thesis, I explore the optical properties of ALD grown ZnO and its suitability for microbolometer applications. By modulation of deposition temperature, the optical characteristics of the deposited films are modified significantly. In addition, a reference microbolometer design is proposed and compared with commercially available materials.

5.2. Optical Properties

Spectroscopic ellipsometry method is exploited to extract the optical properties of atomic layer deposited ZnO. ZnO is known to have an extinction coefficient (k) close to zero at the wavelengths above its band-edge. For such films, Cauchy dispersion model, which is suitable for characterization of transparent thin films [78], can be used. Initially, this model is employed within the 400-1700nm spectrum in order to find film thickness. The formulation for the refractive index and the extinction coefficient in Cauchy dispersion model is as follows:

$$n(\lambda) = A + \frac{B}{\lambda^2} + \frac{C}{\lambda^4} \tag{6.1}$$

$$k(\lambda) = A_k e^{E_k(\frac{hc}{\lambda} - E_b)} \tag{6.2}$$

where A, B, C, A_k and E_k are fit parameters for the model and E_b is the band edge which is assumed to be 3.37eV. In Table 5.1, the corresponding parameters resulting the best fit along with the film thicknesses are given.

Growth Temperature	Thickness (nm)	A	B $[x10^{-2}]$	C $[x10^{-4}]$	A_k $[x10^{-2}]$	E_k (eV)
80 ^oC	38.5	1.818	4.37	4.13	4.55	1.73
120 ^oC	45.5	1.816	5.05	3.92	4.68	1
200 ^oC	44.9	1.813	4.74	2.84	2.8	0.2
250 ^oC	34.6	1.786	3.03	2.84	2.18	0.229

Table 5.1 - Cauchy parameters for different ZnO deposition temperatures within 400 - 1700nm spectrum.

It is known that the infrared spectrum is generally sensitive to free carrier effects; therefore, the inclusion of free carrier effects is crucial. Drude oscillator is known to model the effect of free carriers for the measured Ψ/Δ spectrum obtained via infrared spectroscopic ellipsometry. In order to accurately model the optical constants within the measured spectrum, 1.8-15μm, a Drude oscillator along with a Lorentz oscillator is utilized as described in the following formulation,

$$\varepsilon(\omega) = \varepsilon'(\omega) + j\varepsilon''(\omega) = \varepsilon_\infty + \varepsilon_{Drude}(\omega) + \varepsilon_{Lorentz}(\omega) \tag{5.3}$$

$$\varepsilon_{Drude}(\omega) = -A \frac{\Gamma}{((\hbar\omega)^2 + j\Gamma\hbar\omega)} \quad (5.4)$$

$$\varepsilon_{Lorentz}(\omega) = A \frac{\Gamma\hbar\omega_n}{(\hbar\omega_n)^2 - (\hbar\omega)^2 - j\Gamma\hbar\omega} \quad (5.5)$$

where $\hbar$ is the Planck's constant, ε_∞ is the static dielectric permittivity, A is the amplitude of the oscillator, Γ is the broadening, ω_n is the center frequency of the oscillator and ω is the frequency.

The IR optical constants are determined by a least square error algorithm using the thickness values listed in Table 5.1 assuming the films as isotropic. As the conductivity of the 80°C grown films is very low, free carrier doesn`t contribute to dielectric constant significantly; therefore, Drude oscillator is neglected for this temperature. In Table 5.2, the values resulting the best fit in parameters of Eqs. (5.3)-(5.5) are listed. The corresponding complex dielectric constants are plotted in Figure 5.1. The amplitude of the Drude oscillator is related to the amount of free carriers within the film. Table 5.2 indicates significant modulation in the amount of free carriers with deposition temperature. On the other hand, the Lorentz oscillator parameters have relatively low variance which is attributed to be small variation in the phonon mode properties of the films by deposition temperature.

Growth Temperature	ε_∞	Lorentz			Drude	
		A	Γ (cm^{-1})	ω_n (cm^{-1})	A (cm^{-1})	Γ (cm^{-1})
80 °C	3.70	35.7	47.07	396.5	-	-
120 °C	3.71	51.2	48.3	397.3	1694	8468
200 °C	3.65	51.6	52.74	397	8109	2024
250 °C	3.25	55.8	60.98	396.5	14886	2241

Table 5.2 – Both Lorentz and Drude oscillator parameters within the infrared spectrum of interest as a function of ZnO deposition temperature.

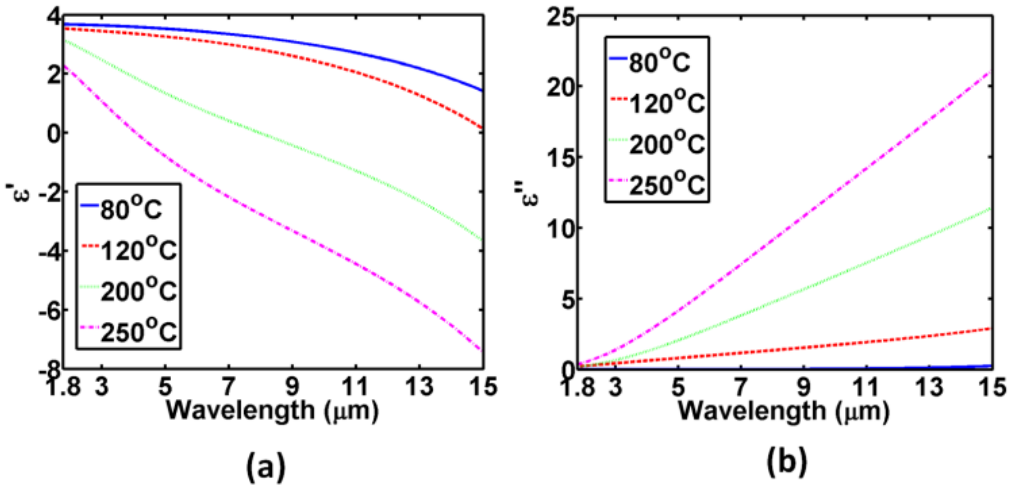

Figure 5.1 - ALD deposited ZnO optical constants for various deposition temperatures. (a) Real (ε') and (b) Imaginary (ε") parts of the dielectric constants of the ALD grown ZnO films is a function of deposition temperature. Metallic behavior becomes dominant at higher temperatures due to increased concentration of free carriers. Copyright 2014 John Wiley and Sons

Absorption properties of the films can be extracted from the imaginary part of the dielectric constant (ε''). Increased deposition temperature results in highly absorptive films which make them suitable for microbolometric applications as high absorption is desired for the application purposes. There is also significant control over the real part of the dielectric constant (ε') by deposition temperature. The plasma wavelength (λ_p) for the materials, at which ε' becomes zero, redshifts for lower deposition temperatures. This indicates lowering of electron concentration; therefore, conductivity. For 120^{o}C and 80^{o}C deposited films, λ_p remains above the wavelength range of interest, noting that 120^{o}C deposited film has higher conductivity compared to 80^{o}C deposited film due to having lower ε' within the entire spectrum. The plasma wavelength for

200^{o}C and 250^{o}C deposited films are 8μm and 4.08μm, respectively; therefore, these films exhibit metallic behavior which can be exploited for dielectric based plasmonics in bolometric applications.

In order to verify the optical constants, Fourier transform infrared (FTIR) reflection spectrum of the as grown ZnO films are measured with respect to the Si reference such that the spectra would indicate reflection from ZnO surface divided by reflection from uncoated Si surface. Simulations of the reflection spectra are performed using the extracted optical constants. The corresponding results for measurements and simulations, which agree very well, are depicted in Figure 5.2.

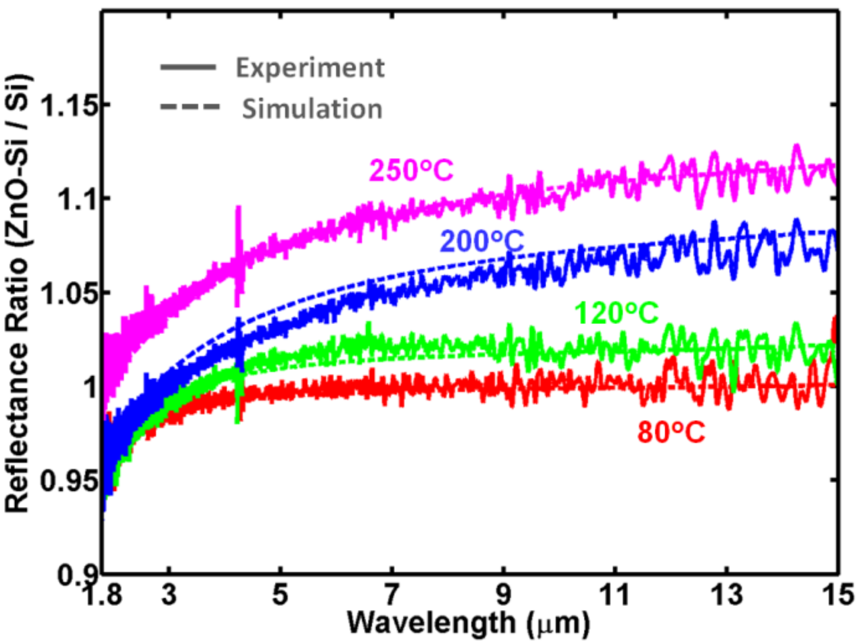

Figure 5.2 – Comparison of FTIR reflection measurements (solid lines) with simulations (dashed lines) using extracted optical constants. The agreement between the measured and simulated spectra indicates the accuracy of the extracted permittivity values. Copyright 2014 John Wiley and Sons

5.3. Device Analysis

In order to get a good knowledge on the absorption performance of the films, a reference bolometer structure [78] made of Si_3N_4, which is the commercial standard, is compared with the deposited films via FDTD simulations. The reference structure consists of an absorber layer above a metallic reflector with an air gap of 2µm as shown in Figure 5.3a [78]. For all of the films, the simulated absorption spectrum calculated as 1-Reflection is depicted in Figure 5.3c. For the spectrum of interest, 8-12µm, all ZnO films exhibit viable absorption characteristics. It is more clear in the integrated absorption plot for 8-12µm in Figure 5.3b such that absorption performance comparable to Si_3N_4 is achieved for all ZnO films except for 80^oC whereas 200^oC deposited ZnO film having 85% absorption exceeds Si_3N_4 by 13% which makes it a very attractive structural material. Due to low ε'' (below 1) of 80^oC deposited ZnO films, there is low absorption for this case; nevertheless, 80^oC deposited films can still be useful an infrared anti-reflective coating due having relatively low refractive index.

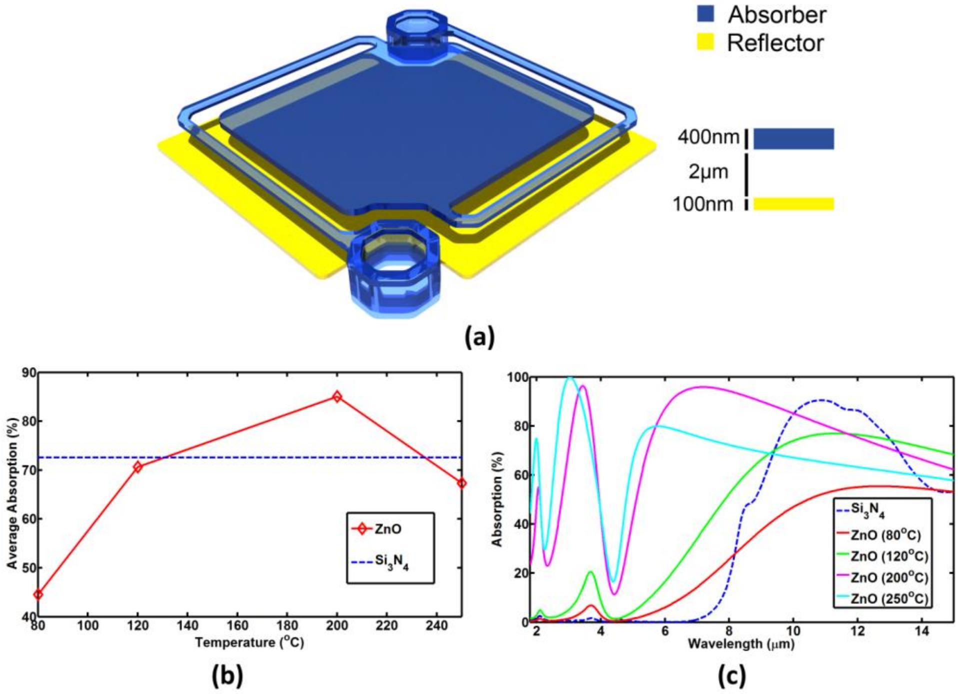

Figure 5.3 - Reference structures depiction with absorption characteristics for different materials. (a) 3D depiction of reference structure. (b) FDTD simulation of average absorption for both ZnO and Si_3N_4 films in 8-12μm spectrum. (c) The spectral absorption for all of the compared films. Copyright 2014 John Wiley and Sons

5.4. Conclusion

Suitability of optical properties of ALD deposited ZnO films for bolometric applications is investigated in this chapter. For various deposition temperature, optical constants of ALD deposited ZnO films are extracted and modeled utilizing Drude and Lorentz oscillators. Since ALD provides modulation of free carrier concentrations by variation of deposition temperatures, the dielectric properties of the films could be manipulated as desired. By incrementing the deposition temperature, ZnO films with absorption performance ranging from relatively low to very high can be obtained. Comparison of the ZnO films with a commercial standard absorber material indicated that 200^{o}C deposited ZnO films perform much better; therefore, become a good candidate for replacing the commercial standard absorber material in microbolometers.

Chapter 6

ZnO as an alternative thermo-optic material

6.1 Introduction

The desired control over light matter interactions resulted in birth of reconfigurable optical structures especially due to expansion of optoelectronic applications within optical computation and communication, display, lighting, imaging, holographic technologies. The most dominant methods of optical modulation is utilization of free-carrier effects, electro-absorption, electro-optic and thermo-optic effects. However, these effects hit the limits in terms of loss, modulation contrast, speed, bandwidth, spectral coverage or integration cost; therefore, search for new schemes has grown. Recently, new optical modulation schemes have been demonstrated such as coupling metamaterials [22], plasmonic gratings [79], optical cavities [80] and photonic crystals [81] with well-known optical modulation media i.e. Silicon [82], GaAs [83], $LiNbO_3$ [84], liquid crystals [85]. On this end, advancements large band-gap electronics attracted attention in their integration to electro-optical applications within visible and ultraviolet spectrum.

In this section of the thesis, atomic layer deposited ZnO is introduced as a new material exhibiting large thermo-optic effects. Active modulation of refractive index is achieved within the UV-VIS-NIR spectrum and demonstrated via realization of a Fabry-Perot cavity exhibiting resonant absorption. By modulating the temperature between 23^{o}C and 200^{o}C, more than 5nm shift in the resonances within UV-VIS-NIR spectrum is achieved. Through spectroscopic ellipsometry, temperature dependent refractive indices of ZnO in 300-1600nm spectrum are extracted. Around the band-edge of ZnO, largest refractive index modulation is observed and the band-edge is redshifted due to thermal expansion. Optical properties of ZnO is also investigated in mid-IR spectrum covering 4-40μm and found out that no significant modulation is obtained. However, the thermal relaxation is verified through the observed red-shift of the optical phonon modes of ZnO. A thermo-optic coefficient of $9.17x10^{-4}/^{o}K$ is obtained around the band-edge which is the largest among the large band-gap materials

6.2. Ellipsometric Characterization

Ellipsometric measurements are performed in UV-VIS-NIR from a Fabry Perot resonant cavity structure formed by coating a 240-nm-thick ZnO layer on top of a p-type silicon wafer with resistivity in the range of 0.1-0.9 Ω-cm. Standard RCA cleaning procedure is carried out before film deposition. Using atomic layer deposition technique, ZnO is coated through 1700 deposition cycles within Cambridge Savannah 100 chamber at $250^{o}C$.

Prior to the ellipsometric measurements, annealing is carried out on the samples at $250^{o}C$ in atmospheric conditions for 90 minutes. A cyclic temperature dependent ellipsometric measurement is carried out while modulating the sample temperature between $23^{o}C$ and $200^{o}C$ with illumination at an angle of incidence of 55^{o} and 57^{o}. A nonlinear least square error fitting algorithm is used to fit oscillator parameters to measured Ψ/Δ values and the mean square error below 3 is aimed during the fit for all temperatures. For each temperature of interest, the optical constants of the underlying Si layer is extracted to eliminate the contribution of refractive index modulation from the Si layer.

Modeling of optical constants of ZnO is performed using a Cody-Lorentz oscillator coupled with two Gaussian oscillators and an un-damped Lorentz oscillator. Cody-Lorentz oscillator is used for accurate modeling of wide-bandgap semiconductors. The contribution of defect states and intra-band absorptions which would result in non-zero absorption below the band-gap in the form of an exponentially decaying function named as Urbach's Tail [86] is included in this model. The corresponding equations for the optical constants are as follows

$$\varepsilon(E) = \varepsilon'(E) + j\varepsilon''(E) \qquad (7.1)$$

$$\varepsilon''(E) = \varepsilon''_{Cody-Lorentz}(E) + \varepsilon''_{Gauss-1}(E) + \varepsilon''_{Gauss-2}(E) + \varepsilon''_{Pole}(E) \qquad (7.2)$$

$$\varepsilon'(E) = \varepsilon_\infty + \varepsilon'_{Pole}(E) + \frac{2}{\pi} P \int_{-\infty}^{\infty} \frac{\xi \varepsilon''(\xi)}{\xi^2 - E^2} d\xi \qquad (7.3)$$

$$\varepsilon'_{Pole}(E) = \frac{A}{E_o{}^2 - E^2} \qquad (7.4)$$

$$\varepsilon''_{Cody-Lorentz}(E) = \begin{cases} \frac{E1}{E} \mathrm{e}^{\frac{(E-Et)}{Eu}}, E < (Eg - Et) \\ \frac{(E-E_g)^2}{(E-E_g)^2 + E^2{}_p} \frac{AE_o \Gamma E}{(E^2 - E^2)^2 + \Gamma^2 E^2}, E > (Eg - Et) \end{cases} \qquad (7.5)$$

$$\varepsilon''_{Gauss}(E) = Ae^{-\left(\frac{\ln 4 (E - E_o)}{\Gamma}\right)^2} - Ae^{-\left(\frac{\ln 4 (E + E_o)}{\Gamma}\right)^2} \qquad (7.6)$$

Eq. (7.1) separates the real and imaginary part of the complex dielectric function; Eq. (7.2) is the total imaginary part of the dielectric function which is modeled by various oscillators listed above; Eq. (7.3) ties the real and imaginary parts of the dielectric permittivity through Kramers-Kronig relationship; Eqs. (7.4-7.6) describe the oscillator equations. In these equations, E stands for photon energy, ε_∞ is the static dielectric constant, E_o stands for the center resonance frequency of the oscillator, Γ is the broadening parameter, A is the oscillator amplitude, E_g is the optical band-gap, E_p is the transition energy separating absorption onset from Lorentzian behavior, E_t is the transition energy between Urbach tail and band-to-band transitions, E_u is the Urbach Energy defining the spectral rate of decay of the absorption and E_1 is a fit parameter providing continuity at $E=E_t$. The extracted parameters are given in Tables 6.1 and 6.2 as a function of temperature. Optical band-gap of the ZnO film is found to be 3.23eV at room-temperature and drops from 3.23eV to 3.10eV for elevation of temperature up to 200^{o}C from 23^{o}C. This lowering of the band-gap is expected as a result of Varshni`s formulation [87] which indicates that increased separation between atoms of the semiconductor as a result of elevated temperature causes narrowing in the band-gap

		ε'_{Pole}		$\varepsilon''_{Cody-Lorentz}$					
T (^oC)	ε_∞	A	E_o (eV)	Γ (eV)	E_g (eV)	E_p (eV)	E_t (eV)	E_u (eV)	E_o (eV)
23	2.24	18.3	3.09	0.105	3.26	0.992	0.0102	1.204	5.35
100	2.46	14.8	2.68	0.147	3.16	1.003	0.0181	1.178	5.30
200	2.39	17.8	2.50	0.156	3.10	1.004	0.0191	0.883	5.40

Table 6.1 – Thermal dependency of Pole and Cody-Lorentz oscillator parameters for ZnO in 300 – 1600 nm spectrum.

	$\varepsilon''_{Gauss-1/2}$		
T (^oC)	A	E_o (eV)	Γ (eV)
23	0.352 / 1.21	3.443 / 3.38	0.405 / 0.140
100	0.777 / 0.944	3.442 / 3.36	0.358 / 0.121
200	0.738 / 0.714	3.424 / 3.32	0.397 / 0.134

Table 6.2 - Thermal dependency of Gaussian oscillator parameters for ZnO in 300 – 1600 nm spectrum.

The extracted thermal dependency of refractive index values of ZnO from $n = \mathrm{Re}\{\sqrt{\varepsilon}\}$ in 300-1600nm spectrum is depicted in Figure 6.1a. Both real and imaginary parts of the refractive index are modulated within the entire spectrum of interest. Repeatability and volatility of the modulation is verified by observation of return of ZnO refractive indices to initial values after thermal stress is removed. As depicted in Figure 6.1b, the refractive index modulation reaches its maximum value of 0.2 at around the band-edge of ZnO which corresponds to a thermo-optic coefficient of $9.17\times10^{-4}/^oK$ exceeding the thermo-optic coefficient of large band-gap semiconductor counterparts such as AlN, GaN, SiC [88] by 4 times in magnitude.

The exciton binding energy for ZnO is about 60meV which is high enough to modify the optical properties visibly around the band edge; therefore, a corresponding sharp peak is observed at the band-edge of the extinction spectra of ZnO in Figure 6.1c. Increasing temperature causes the excitonic peak to red-shift and get lower in the amplitude as the available kinetic energy gets a value closer to the binding energy of excitons resulting in weakening of the photon-exciton resonance strength.

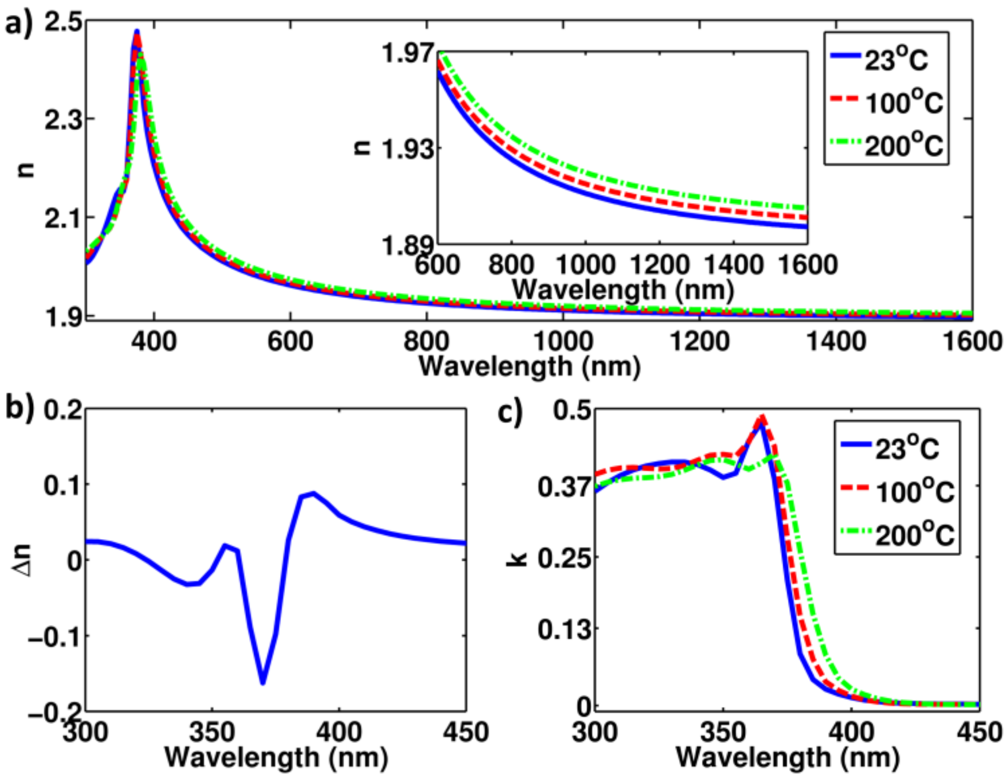

Figure 6.1 – Near visible optical constants of the ZnO film. a) Thermal dependence of the real part of the refractive index in 300-1600nm spectrum. The inset shows the sub-bandgap region. b) Variation in the refractive index for temperature increase from 23°C to 200°C. c) Thermal dependence of extinction spectra showing red-shift of the band-edge due to thermal expansion

Below the band-edge, the maximum modulation of refractive index is about 0.01 which is lower than the values around the band-edge. This is a strong indication of involvement of thermally modifiable exciton-photon interactions around the band-edge. Moreover, the increase in the temperature lowers the occupation probability of the trap-states resulting in more trap-state related absorption which is reflected as decrease in the value of E_u and an increase in the extinction coefficient of ZnO by 0.002. Above the band-edge, a maximum of 0.02 modulation in the refractive index is still present and attributed to the active modification of density of states due to thermal relaxation.

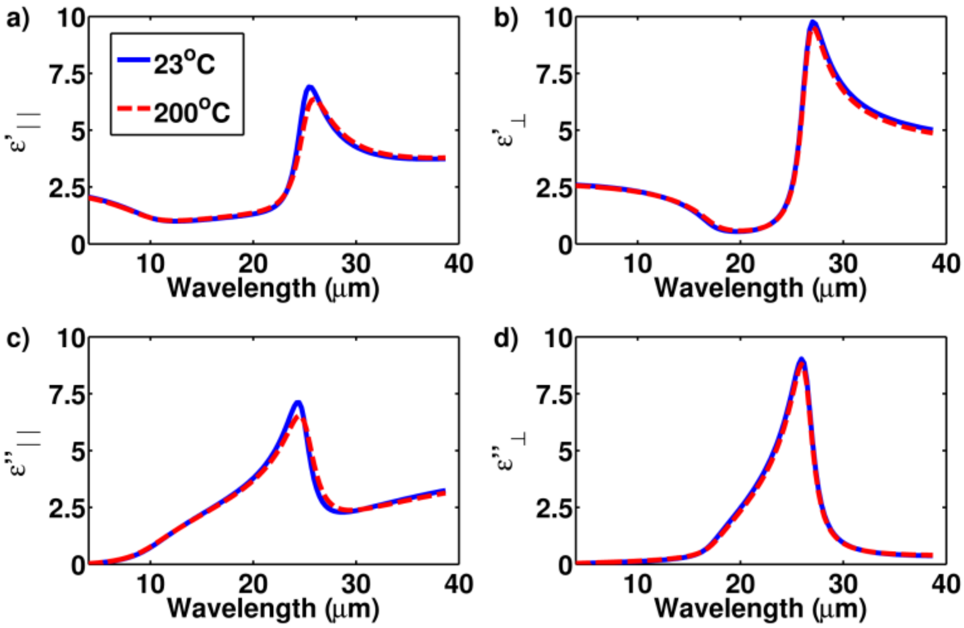

Figure 6.2 – IR optical constants of ZnO films. a-b) Real and c-d) imaginary parts of the mid-infrared anisotropic dielectric constants of ZnO for in-plane and out-of-plane directions, respectively.

Temperature dependent refractive index of ZnO in mid-IR spectrum covering 4-40µm is investigated. It is known that optical phonon modes as well as free-carriers contribute to the dielectric permittivity within this spectrum. To achieve accurate modeling of these effects, a TO-LO oscillator for phonon modes is coupled with a Drude oscillator which accounts for the unintentional n-type doping of ZnO exceeding negligible values, 10^{16} cm^{-3}. The polycrystalline nature of the grown films required to consider anisotropy in the films. The corresponding equations describing the dielectric function in this range are as follows

$$\varepsilon(E) = \varepsilon_{Drude}(E) + \varepsilon_{TO-LO}(E) \quad (7.7)$$

$$\varepsilon_{Drude}(E) = -A\frac{\Gamma}{E^2 + j\Gamma E} \quad (7.8)$$

$$\varepsilon_{TO-LO}(E) = A\frac{E_{LO}^2 - E^2 + j\Gamma E}{E_{TO}^2 - E^2 + j\Gamma E} \quad (7.9)$$

where E_{LO} and E_{TO} stands for the longitudinal and transverse phonon oscillation energy

The parameters resulting the best fit are given in Table 6.3. To account for the uni-axial anisotropy, the optical constants are separated into out-of-plane (⊥) and in-plane (||) parts. Due to insensitivity of spectroscopic ellipsometry to $E_{TO\perp}$ and $E_{LO||}$ values for the film thicknesses less than 1µm, literature values are used. A carrier concentration of 1.07×10^{19} cm^{-3} is extracted and agrees well with the literature [89].

T (°C)	Anisotropy Axis	ε_{Drude} A	ε_{Drude} Γ (eV)	$\varepsilon_{TO\text{-}LO}$ A	$\varepsilon_{TO\text{-}LO}$ E_{LO} (cm^{-1})	$\varepsilon_{TO\text{-}LO}$ E_{TO} (cm^{-1})	$\varepsilon_{TO\text{-}LO}$ Γ (cm^{-1})
23	||	0.924	0.0664	4.993	590	401.7	34.22
	⊥	0.0669	0.917	6.997	584	378	27.17
200	||	0.875	0.0702	4.855	590	397.6	41.48
	⊥	0.0772	0.795	6.824	576.5	378	26.64

Table 6.3 – IR oscillator parameters for the temperature dependent optical constants of ZnO.

Figure 6.2 shows the permittivity values as a function of temperature for the infrared region of the spectrum. No significant modulation in the permittivity values are observed except the region where phonon modes are located, about 27µm. Thermal expansion of the film causes the in-plane phonon modes to red-shift by 100nm. The anisotropy of the dielectric constants of the films disappear at the shorter wavelengths and gets stronger around the wavelengths where phonon modes are located since these modes are strongly dependent on the direction of the incident field.

6.3. Actively Tunable Surface

By forming a thin optical structure that is comparable to the wavelength of incidence, a Fabry Perot (FP) resonance can be achieved within an optical cavity. In this study, the thickness of the ZnO layer is adjusted to achieve constructive interference of the field within the cavity for which the mechanism is depicted in Figure 6.3a. Using the following formula, the reflection spectrum can be extracted for the cavity

$$R = \left| r_1 + \frac{t_1 t_2 r_2 e^{j2n_{ZnO}kd}}{1 - r_2 r_3 e^{-j2n_{ZnO}kd}} \right|^2 \quad (6.10)$$

where *r* and *t* corresponds to Fresnel reflection and transmission coefficients at the corresponding boundaries depicted in Figure 6.3a. For the room temperature (23^{o}C),

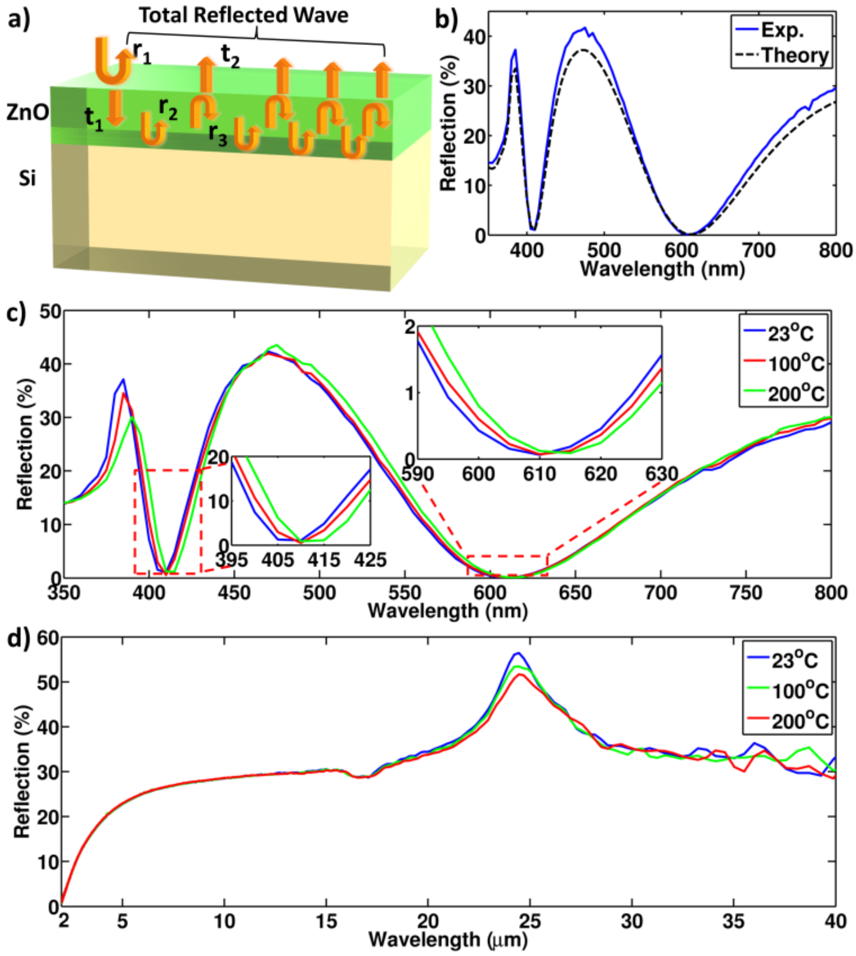

Figure 6.3 – Device structure with reflection characteristics as a function of temperature. a) Depiction of Fabry-Perot resonance mechanism. b) The measured reflection spectrum at the angle of incidence of 20^o and p-polarization along with the theoretical calculation. c) Thermo-optic modulation of FP-resonance. d) No significant modulation in mid-IR regime.

the reflection spectrum in UV-VIS-NIR range for 20^o angle of incidence and p-polarization is shown in Figure 6.3b along with the theoretical calculation using Eq.

(6.10) and the extracted optical constants in Figure 6.1a. Using the extracted refractive indices of ZnO, room temperature FP resonance locations are predicted as 407nm and 610nm which agree well with the experimental results. These wavelengths correspond to the second and third order FP resonances, formulated by $d = (2m+1)(\lambda/4n_{ZnO})$ where m is an integer.

Figure 6.3c shows the reflection spectrum below mid-IR regime as a function of temperature. More than 5nm resonance shift is observed as a result of thermo-optic modulation of refractive index. The shift in the spectra around the band-edge is higher, 10nm, despite having no resonance around the band-edge. This observation is as a result of higher refractive index modulation around the band-edge.

Thermal dependence of the reflection spectrum is also investigated for mid-IR spectrum at 25^o angle of incidence and the corresponding measurements are plotted in Figure 6.3d. The spectrum shows the first order FP-resonance partially near 2µm wavelength. No FP resonance is observed above 2µm wavelength as the structure dimensions remains below sub-wavelength regime. Only $E_{LO\perp}$ and $E_{TO\parallel}$ phonon modes located at 17.1µm and 24.9µm, respectively, are observable and red-shift by 100nm in agreement with the ellipsometric measurements.

6.4. Conclusion

Atomic layer deposited ZnO is investigated as an alternative thermo-optic material in UV-VIS-NIR-MIR range of the spectrum. Temperature dependent optical constants of the ZnO film are extracted using spectroscopic ellipsometry. Below the MIR spectrum, refractive index modulation reached up to 0.2 for a temperature difference of 177^{o}C which exceeded the values for well known large-band-gap materials. In MIR spectrum no significant modulation of refractive index is observed except the region where phonon modes are dominant. The phonon modes are observed to red-shift by 100nm. As a proof-of-concept, the deposited film is measured as an actively tunable reflector surface exhibiting more than 5nm spectral shift due to FP resonances and large refractive index modulation around the band-edge.

Chapter 7

Electro-optic modulation using a novel mechanism: resistive switching

This chapter is based in part on the publication "Atomic-layer-deposited zinc oxide as tunable uncooled infrared microbolometer material," **E. Battal**, A. Ozcan and A. K. Okyay, Advanced Optical Materials Vol. 2, Issue 12, pp.1149-1154 (2014). Reproduced (or 'Reproduced in part') with permission from John Wiley and Sons Publishing Group. Copyright 2014 John Wiley and Sons

7.1. Introduction

Switching between two or more resistance states in a non-volatile fashion is called resistive switching and these devices have simple nature, fast switching speed, high retention times, low power consumption, CMOS compatibility and scalability [90-93]. These properties along with the abundance of suitable materials [94-98] attracted great attention in the research community. These devices exhibit atomic scale modifications [99]; yet, there is no report in their suitability for optical modulation. Since atomic scale modifications are expected to modulate the complex refractive index of the active dielectric, resistive switching can be suitable for electro-optical modulation applications.

In this chapter of the thesis, I investigate resistive switching as an alternative electro-optic modulation technique. A reflector device exhibiting non-volatile and hysteretic modulation of reflection spectrum by 4% in the 5-18µm spectrum is realized. The resistive switching device exhibit repeatable electrical switching over 100 switching cycles. The mechanism providing optical modulation is modeled as variation in the effective doping concentration in the active device material due to reported presence variation in local stoichiometry [99]. The modeling is performed via FDTD simulations using the refractive index values of highly and lowly doped ZnO film refractive indices. Effective doping concentration of the active layer is shown to modulate significantly to effect dielectric permittivity.

7.2. Device structure

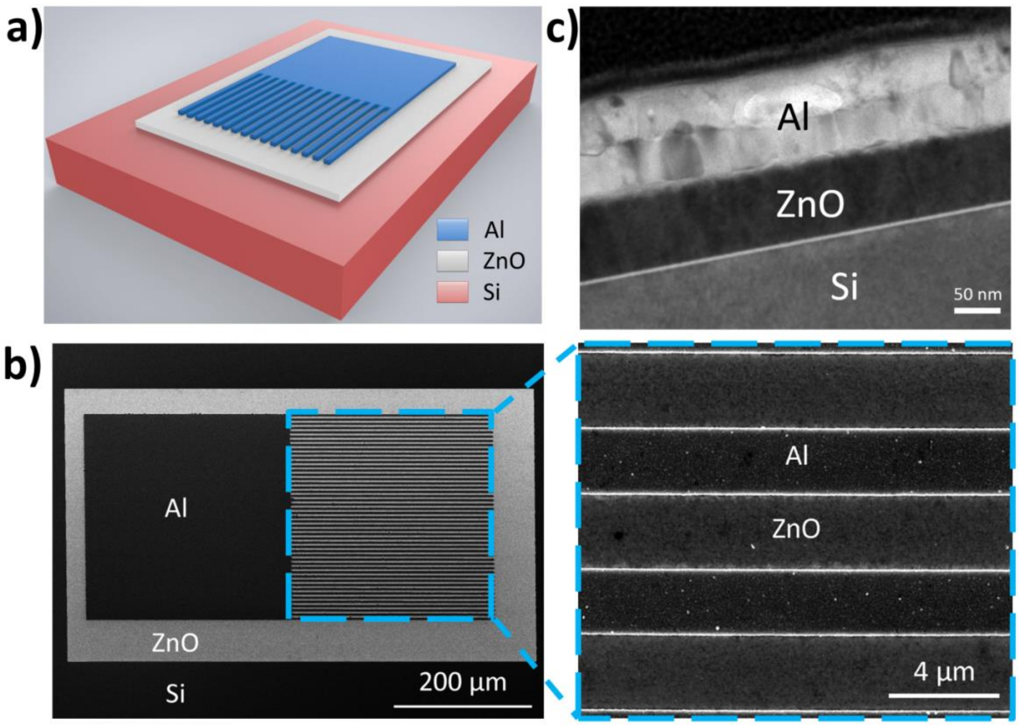

Figure 7.1 – Resistive switching device structure. a) 3-D illustration of the resistive switching device consisting of a dielectric ZnO film in between an aluminium and a highly doped Silicon layer (p-type with resistivity of 3.1mΩ-cm). b) Top view SEM image of the fabricated device. Top aluminium electrode layer consists of a contact pad region along with digitated fingers for optical reflection measurements c) TEM cross section image of the device shows 80-nm-thick ZnO and 120-nm-thick Al layers on top of Si. Copyright 2014 John Wiley and Sons

The resistive switching device structure consists of stacking of Al/ZnO/Si layers as shown in Figure 7.1a. Top and bottom electrodes are Al and highly doped p-type Si layers. An island of dielectric ZnO layer is formed to isolate the device and the top Al layer is patterned to form electrical contact pad with digitated optical measurement region. The device area is 300x600µm^2 and the corresponding SEM image is shown in Figure 7.1b. The top electrode consists of two regions, half the contact pad and half the electro-optic region with gratings having width of 2.43µm and distance of 2.8µm, for which, the TEM cross sectional image is shown in Figure 7.1c.

7.3. Electrical characterization

Electrical properties of the resistive switching device are characterized through straightforward current-voltage (I-V) measurements. Electrical bias is applied from the top electrode while the bottom Si layer is grounded. The current flow from the fresh devices is on the order of 100µA/cm^2. Resistive switching behavior is achieved via a controlled breakdown process which is named as electroforming and performed by employing high electrical voltages to the device. Electroforming allows the resistive switching devices to have atomic scale modifications such as increase of conductivity of the films due to formation of filamentary conducting paths via electric field induced redox reactions [100] and Joule heating [101] as well as zinc and oxygen ion migration [102]. In order to prevent permanent breakdown of the device, the applied power is limited through current flow. In this study, electroforming is performed with a voltage bias of -6V for 1 second duration with a current compliance of 100mA. Repeatable resistive switching is obtained by applying a dual voltage bias sweep between -6 and 6V with again 100mA current compliance. As expected from a resistive switching device, the I-V characteristics of the device shows a hysteresis loop as depicted in the switching cycle of the device in Figure 7.2a. The switching cycle starts by having the device stay at high resistance state (HRS) during the voltage sweep from -6 to 6V until the voltage bias becomes the set voltage (V_{set}) of 2.4V. At this point, a sudden increase in the current amplitude occurs and the device hits to the current compliance going into low resistance state (LRS). In high-resolution transmission electron microscope

(HRTEM) images of the device at LRS, Figure 7.2b, there is clear presence of conducting filaments reaching from the top electrode to the bottom Si substrate, which are responsible for most of the current flow. The filaments in this figure have trapezoidal shape which indicates that the mobile oxygen ions move towards the bottom Si layer during the switching

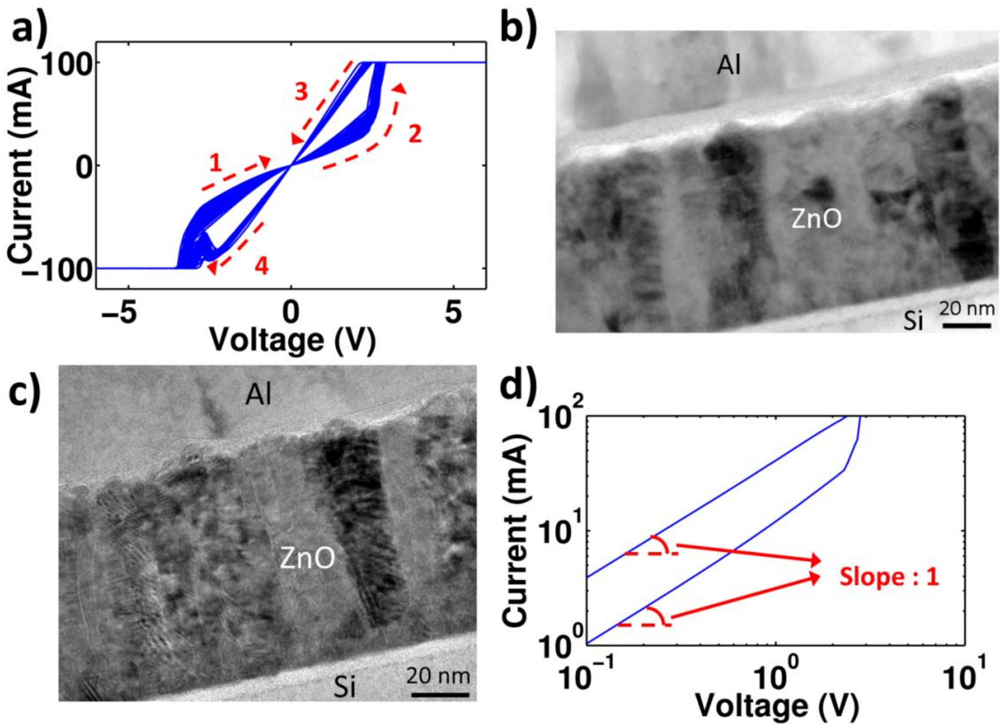

Figure 7.2 - Electrical characteristics of the Al/ZnO/Si resistive switch device along with TEM images for different memory states. a) I-V characterization of the device exhibiting more than 100 cycles of resistive switching. b) HRTEM cross sectional image of the device at LRS depicting thorough filaments from the top electrode to the bottom. c) When the device switches back to HRS, some of the filaments partially dissolve and cause increase in the resistivity d) For all memory states, ohmic conduction with a slope of 1 is present in log-log I-V curve. Copyright 2014 John Wiley and Sons

process [103]. Continuing the voltage sweep from 6 to -6V, the device switches back to HRS with a sharp decrease in the current at -2.4V reset voltage (V_{reset}).

Since the polarity of V_{set} and V_{reset} are different, the device is said to exhibit bipolar resistive switching. After the device switches back to HRS, filaments with partially dissolved regions are observed in the HRTEM cross-sectional image in Figure 7.1c and theorized to decrease the conductivity of the device. Although some filaments are partially dissolved, there are remaining thorough filaments which significantly contribute to conduction preventing high insulation. Thus, the device shows a low contrast ratio between resistance states (R_{HRS}/R_{LRS}) of 3. The described switching cycle is obtained for more than 100 cycles. The stability of the device is remarkable with V_{set} and V_{reset} varying less than 0.3V and the hysteresis curve following the previous cycles quite well as depicted in Figure 7.2a. In order to clarify the conduction mechanism, log-log I-V curve for the device is plotted in Figure 7.2d and the slope of the curve for both resistance states gives 1 which is a strong indication of ohmic conduction. The observed ohmic conduction in both states can be attributed to the presence of thorough filaments [104].

7.4. Optoelectronic characterization

Using a Fourier transform infrared (FTIR) spectrometer, the electroo-optical characterization of the device is performed through reflection measurements from the digitated finger area shown in Figure 7.1b while the device is under electrical bias. The resistive switching device repeats its hysteretic behaviour in the reflection measurements as well. For the wavelength of 8 µm, at which the change in the reflection amplitude is maximum, Figure 7.3a shows the hysteretic reflection amplitude as a function of voltage which is cycled between -6 and 6V. The modulation of reflection remains below 1% until the voltage bias reaches 4V while going from 0V to 6V at LRS. The modulation suddenly increases to 4% right after the voltage bias goes above 4V. At this point, the device is already at HRS. Going back to 0V from 6V, the reflection remains nearly the same; however, below 0V, a linear increase in the reflection occurs towards the original value at LRS. In order to test the non-volatility of the behaviour, the reflection measurements at different states are performed while the voltage bias is removed and observed that the reflection amplitude does not change after the bias is removed. Thus, it can be concluded that the dielectric permittivity of the active layer, ZnO, gets modified in a non-volatile fashion via resistive switching which provides atomic scale modifications. Throughout the 5-18μm spectrum, non-volatile modulation of the reflection spectrum is also observed by 4% for different states under zero electrical bias as depicted in Figure 7.3b.

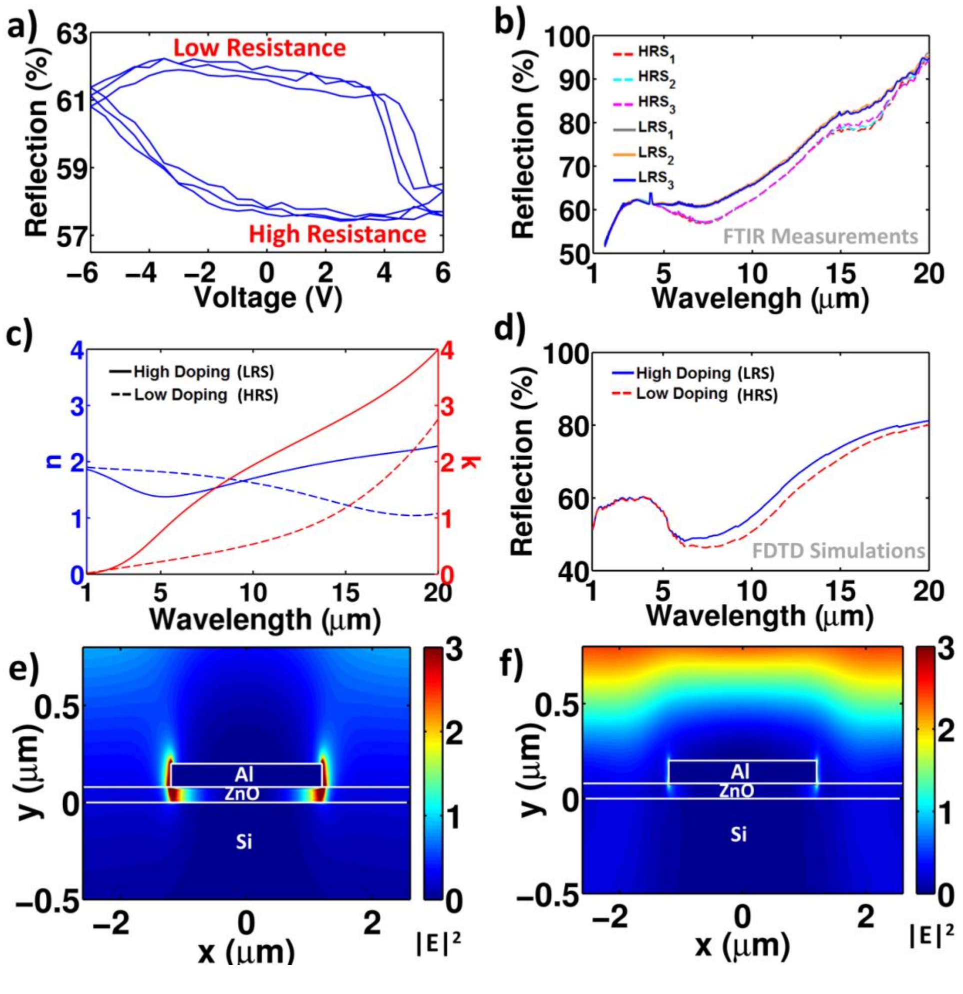

Figure 7.3. Electro-optic characterization and theoretical modelling of the device. a) Electro-optic hysteresis behaviour in the reflection spectrum at 8μm wavelength. b) Broadband non-volatile reflection modulation by 4% in the entire 5-18μm spectrum c) Extracted modulation of optical constants through FDTD simulations and modelling the variation of effective doping concentration between

4.4x10^{19} cm^{-3} and 3.84x10^{19} cm^{-3} d) Simulated reflection spectra including the effect of modulation of effective doping concentration e) Strong localization within ZnO dielectric layer in electric field intensity profile for the wavelength of 14µm. f) Comparably lower localization of the incident filed in the case for 4µm. Copyright 2014 John Wiley and Sons

Since resistive switching is known to generate modifications in local stochiometry within an oxide based dielectric [103], in turn, modulate effective doping concentration of the dielectric [105, 106];, variation of the dielectric constants is expected [107]. Drude theory of free carriers theorizes that doping or free carrier concentration affects the optical constants of dielectric especially known to be effective above the near infrared spectrum [107]. To accurately look for the effects of modulation of doping concentration, optical constants of ZnO films with doping concentrations between 10^{16} cm^{-3} up to 10^{21} cm^{-3} are extracted. Using these values, FDTD simulations have been performed to fit the experimental reflection spectrum. During the simulations, available literature values [108] for the p-type silicon with resistivity of 3.1 mΩ-cm is used. Best fitting doping concentrations of 3.84x10^{19} for HRS and 4.4x10^{19} cm^{-3} for LRS, for which the refractive index values are plotted in Figure 7.3c. Very good agreement between the simulation results for the reflection spectrum in Figure 7.3d and that of experimental results in Figure 7.3b. Similar to the experimental results, 4% modulation in the reflection spectra within 5-18µm spectrum lower than 1% below 5 µm is. When the field intensity profiles at 4µm and 14µm in Figure 7.3e and 7.3f, respectively, are investigated, it becomes clear that higher field localization; therefore, higher interaction, in the active layer at higher wavelengths makes it more affected by the refractive index modulation due to resistive switching. The accuracy in the modelling of the modulated reflection spectrum with the variation in the effective doping concentrations through FDTD simulations indicates that the local stoichiometry is modified at different resistance states and therefore the effective doping concentration of the film.

7.5. Conclusion

Resistive switching is demonstrated as a novel electro-optic modulation method. A proof-of-concept device is demonstrated via realizing a stack of Al/ZnO/Si layers exhibiting resistive switching behavior. Using FTIR measurements while having the device under electrical bias, electro-optical modulation of reflection spectrum by 4% within 5-18μm spectrum is observed. The resistive switching mechanism of the device is shown to be formation and rupture of conductive filamentary regions via TEM images. Taking modification of local stoichiometry into account, the observed electro-optic modulation is theoretically modeled through effect of effective doping concentration on dielectric permittivity. As a result of this study, resistive switching mechanism is tied with optical modulation schemes as a new method and pave the way for realizing non-volatile optical memory devices.

Conclusion

Plasmonics is investigated in terms of novelty in applications and also in material. A new method of beam steering utilizing a plasmonic resonator called metal-insulator-metal is introduced. By forming a phased array antenna out of these resonators with slightly different structural dimensions and controlling the refractive index of the insulator layer, active beam steering is demonstrated theoretically within the infrared spectrum. Beam steering range up to 8.75^{o} is achieved by refractive index variation of about 0.15. Beam steering is not limited to a single frequency but achieved within 650nm spectrum around 10μm wavelength while the beam steering range remains nearly the same.

Material aspects of plasmonics is explored through demonstration of a new free carrier rich material, HPCVD grown InN, as a surface plasmon bearing dielectric. Mid-IR optical constants of InN is extracted using spectroscopic ellipsometry and optical characteristics as well as surface plasmon characteristics such as plasmon propagation loss and mode size is investigated and compared with that of Au. A proof-of-concept plasmonic device made out of InN gratings have been realized to show that a strongly resonant absorber surface can be achieved with InN supportin various plasmonic modes.

Investigation of novel materials covers more than half of this thesis. Atomic layer deposited ZnO films are investigated for micro-bolometric applications within the infrared region of the spectrum through extraction of the optical properties of the films at various deposition temperatures. Well-known Drude and Lorentz oscillators have been utilized while modelling the dielectric constants of the films and observed that the amount of the free carrier concentration within the films contribute significantly to the optical properties and can be modulated via deposition temperature. Thanks to controllable optical properties of ZnO films, reference bolometer device utilizing this novel material have been theoretically shown to exceed the integrated absorption performance of the commercially standard material.

Then, ZNO films are investigated for their suitability in thermos-optic applications within the visible and infrared region of the spectrum through, again, spectroscopic ellipsometry. By modulating the temperature of a ZnO film, the temperature dependent refractive index of ALD grown ZnO films have been extracted. A maximum modulation of about 0.2 with only 177^{o}C temperature difference is achieved and observed to be larger than that of the large-bandgap counterparts in the near visible range of the spectrum. In the IR range, optical constants indicated red-shift in the phonon-modes of ZnO as a result of thermal expansion.

Finally, resistive switching, which is modulation of resistance of an electrical device between different values in a non-volatile fashion, is explored for opto-electronic applications. An electro-optic modulator is constructed by stacking Al/ZnO/Si layers which forms a device exhibiting stable resistive switching. Through reflection measurements under electrical bias, up to 4% modulation in the reflection spectrum is observed throughout mid-IR spectrum. Formation and dissolution of the filaments, which modify local stoichiometry, are observed in TEM studies. Therefore, the modulated refractive index is modeled as a result of variation in the effective doping concentration and very good agreement between the theoretical and experimental results is achieved.

Bibliography

[1] H. A. Atwater and A. Polman, "Plasmonics for improved photovoltaic devices," *Nat Mater*, vol. 9, pp. 205-213, 2010.

[2] S. Pillai and M. A. Green, "Plasmonics for photovoltaic applications," *Solar Energy Materials and Solar Cells*, vol. 94, pp. 1481-1486, 2010.

[3] E. Battal, T. A. Yogurt, L. E. Aygun, and A. K. Okyay, "Triangular metallic gratings for large absorption enhancement in thin film Si solar cells," *Optics Express*, vol. 20, pp. 9458-9464, 2012/04/23 2012.

[4] J. A. Shackleford, R. Grote, M. Currie, J. E. Spanier, and B. Nabet, "Integrated plasmonic lens photodetector," *Applied Physics Letters*, vol. 94, p. 083501, 2009.

[5] J. Hetterich, G. Bastian, N. A. Gippius, S. G. Tikhodeev, G. von Plessen, and U. Lemmer, "Optimized Design of Plasmonic MSM Photodetector," *Quantum Electronics, IEEE Journal of*, vol. 43, pp. 855-859, 2007.

[6] F. B. Atar, E. Battal, L. E. Aygun, B. Daglar, M. Bayindir, and A. K. Okyay, "Plasmonically enhanced hot electron based photovoltaic device," *Optics Express*, vol. 21, pp. 7196-7201, 2013/03/25 2013.

[7] P. Jain, X. Huang, I. El-Sayed, and M. El-Sayed, "Review of Some Interesting Surface Plasmon Resonance-enhanced Properties of Noble Metal Nanoparticles and Their Applications to Biosystems," *Plasmonics*, vol. 2, pp. 107-118, 2007/09/01 2007.

[8] J. Lakowicz, "Plasmonics in Biology and Plasmon-Controlled Fluorescence," *Plasmonics*, vol. 1, pp. 5-33, 2006/03/01 2006.

[9] G. Lozano, D. J. Louwers, S. R. K. Rodriguez, S. Murai, O. T. A. Jansen, M. A. Verschuuren, and J. Gomez Rivas, "Plasmonics for solid-state lighting: enhanced excitation and directional emission of highly efficient light sources," *Light Sci Appl*, vol. 2, p. e66, 2013.

[10] R. M. Bakker, H.-K. Yuan, Z. Liu, V. P. Drachev, A. V. Kildishev, V. M. Shalaev, R. H. Pedersen, S. Gresillon, and A. Boltasseva, "Enhanced localized fluorescence in plasmonic nanoantennae," *Applied Physics Letters*, vol. 92, p. 043101, 2008.

[11] R. F. Oulton, V. J. Sorger, D. A. Genov, D. F. P. Pile, and X. Zhang, "A hybrid plasmonic waveguide for subwavelength confinement and long-range propagation," *Nat Photon*, vol. 2, pp. 496-500, 2008.

[12] J. Grandidier, G. C. des Francs, S. Massenot, A. Bouhelier, L. Markey, J.-C. Weeber, C. Finot, and A. Dereux, "Gain-Assisted Propagation in a Plasmonic Waveguide at Telecom Wavelength," *Nano Letters*, vol. 9, pp. 2935-2939, 2009/08/12 2009.

[13] J. A. Dionne, K. Diest, L. A. Sweatlock, and H. A. Atwater, "PlasMOStor: A Metal−Oxide−Si Field Effect Plasmonic Modulator," *Nano Letters*, vol. 9, pp. 897-902, 2009/02/11 2009.

[14] D. Pacifici, H. J. Lezec, and H. A. Atwater, "All-optical modulation by plasmonic excitation of CdSe quantum dots," *Nat Photon*, vol. 1, pp. 402-406, 2007.

[15] Y. Kim, S. Kim, H. Jung, E. Lee, and J. W. Hahn, "Plasmonic nano lithography  with a high scan speed contact probe," *Optics Express*, vol. 17, pp. 19476-19485, 2009/10/26 2009.

[16] L. Pan, Y. Park, Y. Xiong, E. Ulin-Avila, Y. Wang, L. Zeng, S. Xiong, J. Rho, C. Sun, D. B. Bogy, and X. Zhang, "Maskless Plasmonic Lithography at 22 nm Resolution," *Sci. Rep.*, vol. 1, 2011.

[17] A. Noor and Z. Hu. (2010, Metamaterial dual polarised resistive Hilbert curve array radar absorber. *IET Microwaves, Antennas & Propagation 4(6),* 667-673. Available: http://digital-library.theiet.org/content/journals/10.1049/iet-map.2009.0047

[18] M. B. Johnston, "Plasmonics: Superfocusing of terahertz waves," *Nat Photon,* vol. 1, pp. 14-15, 2007.

[19] H. Kang, C.-J. Heo, H. C. Jeon, S. Y. Lee, and S.-M. Yang, "Durable plasmonic cap arrays on flexible substrate with real-time optical tunability for high-fidelity SERS devices," *ACS Applied Materials & Interfaces,* vol. 5, pp. 4569-4574, 2013/06/12 2013.

[20] G. T. Reed, G. Mashanovich, F. Y. Gardes, and D. J. Thomson, "Silicon optical modulators," *Nat Photon,* vol. 4, pp. 518-526, 2010.

[21] B. Sensale-Rodriguez, R. Yan, M. M. Kelly, T. Fang, K. Tahy, W. S. Hwang, D. Jena, L. Liu, and H. G. Xing, "Broadband graphene terahertz modulators enabled by intraband transitions," *Nat Commun,* vol. 3, p. 780, 2012.

[22] I. M. Pryce, K. Aydin, Y. A. Kelaita, R. M. Briggs, and H. A. Atwater, "Highly Strained Compliant Optical Metamaterials with Large Frequency Tunability," *Nano Letters,* vol. 10, pp. 4222-4227, 2010/10/13 2010.

[23] R. M. Briggs, I. M. Pryce, and H. A. Atwater, "Compact silicon photonic waveguide modulator based on the vanadium dioxide metal-insulator phase transition," *Optics Express,* vol. 18, pp. 11192-11201, 2010/05/24 2010.

[24] R. A. Soref and B. R. Bennett, "Electrooptical effects in silicon," *Quantum Electronics, IEEE Journal of,* vol. 23, pp. 123-129, 1987.

[25] J. Komma, C. Schwarz, G. Hofmann, D. Heinert, and R. Nawrodt, "Thermo-optic coefficient of silicon at 1550 nm and cryogenic temperatures," *Applied Physics Letters,* vol. 101, pp. -, 2012.

[26] J. Pfeifle, L. Alloatti, W. Freude, J. Leuthold, and C. Koos, "Silicon-organic hybrid phase shifter based on a slot waveguide with a liquid-crystal cladding," *Optics Express,* vol. 20, pp. 15359-15376, 2012/07/02 2012.

[27] V. V. Temnov, "Ultrafast acousto-magneto-plasmonics," *Nat Photon,* vol. 6, pp. 728-736, 2012.

[28] R. B. Li, L. Deng, and E. W. Hagley, "Fast, all-optical, zero to π continuously controllable Kerr phase gate," *Physical Review Letters,* vol. 110, p. 113902, 2013.

[29] Y. Lu, L. Liu, D. Mandler, and P. S. Lee, "High switching speed and coloration efficiency of titanium-doped vanadium oxide thin film electrochromic devices," *Journal of Materials Chemistry C,* vol. 1, pp. 7380-7386, 2013.

[30] Y. C. Yang, F. Pan, Q. Liu, M. Liu, and F. Zeng, "Fully room-temperature-fabricated nonvolatile resistive memory for ultrafast and high-density memory application," *Nano Letters,* vol. 9, pp. 1636-1643, 2009/04/08 2009.

[31] L. Heng-Yuan, C. Pang-Shiu, W. Ching-Chiun, M. Siddheswar, T. Pei-Jer, L. Cha-Hsin, L. Lurng-Shehng, and T. Ming-Jinn, "Low-power switching of nonvolatile resistive memory using hafnium oxide," *Japanese Journal of Applied Physics,* vol. 46, p. 2175, 2007.

[32] Y. Kane, "Numerical solution of initial boundary value problems involving maxwell's equations in isotropic media," *Antennas and Propagation, IEEE Transactions on,* vol. 14, pp. 302-307, 1966.

[33] N. S. Holliman, N. A. Dodgson, G. E. Favalora, and L. Pockett, "Three-Dimensional Displays: A Review and Applications Analysis," *IEEE Transactions on Broadcasting*, vol. 57, pp. 362-371, 2011.
[34] R. Keil, M. Heinrich, F. Dreisow, T. Pertsch, A. Tunnermann, S. Nolte, D. N. Christodoulides, and A. Szameit, "All-optical routing and switching for three-dimensional photonic circuitry," *Science Reports*, vol. 1 2011.
[35] H.-C. Jau, T.-H. Lin, R.-X. Fung, S.-Y. Huang, J. H. Liu, and A. Y. G. Fuh, "Optically-tunable beam steering grating based on azobenzene doped cholesteric liquid crystal," *Optics Express*, vol. 18, pp. 17498-17503, 2010.
[36] M. Holz and W. C. Goltsos, "Agile beam steering using binary optics microlens arrays," *Optical Engineering*, vol. 29, pp. 1392-1397, 1990.
[37] M. Jarrahi, R. F. W. Pease, D. A. B. Miller, and T. H. Lee, "Optical switching based on high-speed phased array optical beam steering," *Applied Physics Letters*, vol. 92, pp. 014106-3, 2008.
[38] J. F. Lotspeich, "Electrooptic light-beam deflection," *IEEE Spectrum*, vol. 5, pp. 45-52, 1968.
[39] Q. Song, S. Campione, O. Boyraz, and F. Capolino, "Silicon-based optical leaky wave antenna with narrow beam radiation," *Optics Express*, vol. 19, pp. 8735-8749, 2011.
[40] V. V. Temnov, "Ultrafast acousto-magneto-plasmonics," *Nature Photonics*, vol. 6, pp. 728-736, 2012.
[41] A. E. Attard, "Analysis of an Optically Controlled Photonic Switch," *Applied Optics*, vol. 38, pp. 3239-3248, 1999.
[42] K. Appavoo and R. F. Haglund, "Detecting Nanoscale Size Dependence in VO2 Phase Transition Using a Split-Ring Resonator Metamaterial," *Nano Letters*, vol. 11, pp. 1025-1031, 2011/03/09 2011.
[43] C. Qiu, X. Ye, R. Soref, L. Yang, and Q. Xu, "Demonstration of reconfigurable electro-optical logic with silicon photonic integrated circuits," *Optics Letters*, vol. 37, pp. 3942-3944, 2012.
[44] D. de Ceglia, M. A. Vincenti, and M. Scalora, "Wideband plasmonic beam steering in metal gratings," *Optics Letters*, vol. 37, pp. 271-273, 2012.
[45] D. C. Adams, S. Thongrattanasiri, T. Ribaudo, V. A. Podolskiy, and D. Wasserman, "Plasmonic mid-infrared beam steering," *Applied Physics Letters*, vol. 96, pp. 201112-3, 2010.
[46] S. I. Bozhevolnyi and T. Søndergaard, "General properties of slow-plasmon resonant nanostructures: nano-antennas and resonators," *Optics Express*, vol. 15, pp. 10869-10877, 2007.
[47] E. D. Palik, *Handbook of Optical Constants of Solids* vol. 3. Orlando: Academic Press, 1985.
[48] G. Cocorullo, M. Iodice, and I. Rendina, "All-silicon Fabry-Perot modulator based on the thermo-optic effect," *Optics Letters*, vol. 19, pp. 420-422, 1994.
[49] Q. Xu and M. Lipson, "All-optical logic based on silicon micro-ring resonators," *Optics Express*, vol. 15, pp. 924-929, 2007.
[50] A. Laser. *CO2 Molecular Radiation & Typical Tunable Laser Spectrum*. Available: http://www.accesslaserco.com/pdf/CO2 Spectrum and Tunable Lasers.pdf
[51] H. A. Atwater and A. Polman, "Plasmonics for improved photovoltaic devices," *Nature Materials*, vol. 9, pp. 205-213, 2010.
[52] M. Piliarik and J. í. Homola, "Surface plasmon resonance (SPR) sensors: approaching their limits?," *Optics Express*, vol. 17, pp. 16505-16517, 2009/09/14 2009.

[53] J. Kyung-Young, F. L. Teixeira, and R. M. Reano, "Au/SiO₂ Nanoring Plasmon Waveguides at Optical Communication Band," *Lightwave Technology, Journal of,* vol. 25, pp. 2757-2765, 2007.

[54] K. Chen, R. Adato, and H. Altug, "Dual-Band Perfect Absorber for Multispectral Plasmon-Enhanced Infrared Spectroscopy," *ACS Nano,* vol. 6, pp. 7998-8006, 2012/09/25 2012.

[55] S. Ayas, H. Güner, B. Türker, O. Ö. Ekiz, F. Dirisaglik, A. K. Okyay, and A. Dâna, "Raman Enhancement on a Broadband Meta-Surface," *ACS Nano,* vol. 6, pp. 6852-6861, 2012/08/28 2012.

[56] D. Wu, N. Fang, C. Sun, X. Zhang, W. J. Padilla, D. N. Basov, D. R. Smith, and S. Schultz, "Terahertz plasmonic high pass filter," *Applied Physics Letters,* vol. 83, pp. 201-203, 2003.

[57] G. V. Naik, J. Liu, A. V. Kildishev, V. M. Shalaev, and A. Boltasseva, "Demonstration of Al:ZnO as a plasmonic component for near-infrared metamaterials," *Proceedings of the National Academy of Sciences,* vol. 109, pp. 8834-8838, June 5, 2012 2012.

[58] S. Franzen, "Surface Plasmon Polaritons and Screened Plasma Absorption in Indium Tin Oxide Compared to Silver and Gold," *The Journal of Physical Chemistry C,* vol. 112, pp. 6027-6032, 2008/04/01 2008.

[59] G. V. Naik, J. L. Schroeder, X. Ni, A. V. Kildishev, T. D. Sands, and A. Boltasseva, "Titanium nitride as a plasmonic material for visible and near-infrared wavelengths," *Optical Materials Express,* vol. 2, pp. 478-489, 2012/04/01 2012.

[60] T.-T. Kang, A. Hashimoto, and A. Yamamoto, "Optical properties of InN containing metallic indium," *Applied Physics Letters,* vol. 92, pp. -, 2008.

[61] T. V. Shubina, N. A. Gippius, V. A. Shalygin, A. V. Andrianov, and S. V. Ivanov, "Terahertz radiation due to random grating coupled surface plasmon polaritons," *Physical Review B,* vol. 83, p. 165312, 2011.

[62] K. Kim, W. R. L. Lambrecht, and B. Segall, "Elastic constants and related properties of tetrahedrally bonded BN, AlN, GaN, and InN," *Physical Review B,* vol. 53, pp. 16310-16326, 1996.

[63] A. G. Bhuiyan, A. Hashimoto, and A. Yamamoto, "Indium nitride (InN): A review on growth, characterization, and properties," *Journal of Applied Physics,* vol. 94, pp. 2779-2808, 2003.

[64] R. L. Olmon, B. Slovick, T. W. Johnson, D. Shelton, S.-H. Oh, G. D. Boreman, and M. B. Raschke, "Optical dielectric function of gold," *Physical Review B,* vol. 86, p. 235147, 2012.

[65] J. S. Dyck, K. Kim, S. Limpijumnong, W. R. L. Lambrecht, K. Kash, and J. C. Angus, "Identification of Raman-active phonon modes in oriented platelets of InN and polycrystalline InN," *Solid State Communications,* vol. 114, pp. 355-360, 2000.

[66] A. Kasic, M. Schubert, S. Einfeldt, D. Hommel, and T. E. Tiwald, "Free-carrier and phonon properties of <i>n</i>- and <i>p</i>-type hexagonal GaN films measured by infrared ellipsometry," *Physical Review B,* vol. 62, pp. 7365-7377, 2000.

[67] M. Schubert, T. E. Tiwald, and C. M. Herzinger, "Infrared dielectric anisotropy and phonon modes of sapphire," *Physical Review B,* vol. 61, pp. 8187-8201, 2000.

[68] G. D. Yuan, W. J. Zhang, J. S. Jie, X. Fan, J. X. Tang, I. Shafiq, Z. Z. Ye, C. S. Lee, and S. T. Lee, "Tunable n-Type Conductivity and Transport Properties of

Ga-doped ZnO Nanowire Arrays," *Advanced Materials,* vol. 20, pp. 168-173, 2008.

[69] Ü. Özgür, Y. I. Alivov, C. Liu, A. Teke, M. A. Reshchikov, S. Doğan, V. Avrutin, S.-J. Cho, and H. Morkoç, "A comprehensive review of ZnO materials and devices," *Journal of Applied Physics,* vol. 98, p. 041301, 2005.

[70] E. M. C. Fortunato, P. M. C. Barquinha, A. C. M. B. G. Pimentel, A. M. F. Gonçalves, A. J. S. Marques, L. M. N. Pereira, and R. F. P. Martins, "Fully Transparent ZnO Thin-Film Transistor Produced at Room Temperature," *Advanced Materials,* vol. 17, pp. 590-594, 2005.

[71] R. L. Hoffman, B. J. Norris, and J. F. Wager, "ZnO-based transparent thin-film transistors," *Applied Physics Letters,* vol. 82, pp. 733-735, 2003.

[72] E. Klaus, "Magnetron sputtering of transparent conductive zinc oxide: relation between the sputtering parameters and the electronic properties," *Journal of Physics D: Applied Physics,* vol. 33, p. R17, 2000.

[73] A. Yamada, B. Sang, and M. Konagai, "Atomic layer deposition of ZnO transparent conducting oxides," *Applied Surface Science,* vol. 112, pp. 216-222, 1997.

[74] Z. K. Tang, G. K. L. Wong, P. Yu, M. Kawasaki, A. Ohtomo, H. Koinuma, and Y. Segawa, "Room-temperature ultraviolet laser emission from self-assembled ZnO microcrystallite thin films," *Applied Physics Letters,* vol. 72, pp. 3270-3272, 1998.

[75] A. Rogalski, "Infrared detectors: an overview," *Infrared Physics & Technology,* vol. 43, pp. 187-210, 2002.

[76] S. Heitsch, C. Bundesmann, G. Wagner, G. Zimmermann, A. Rahm, H. Hochmuth, G. Benndorf, H. Schmidt, M. Schubert, M. Lorenz, and M. Grundmann, "Low temperature photoluminescence and infrared dielectric functions of pulsed laser deposited ZnO thin films on silicon," *Thin Solid Films,* vol. 496, pp. 234-239, 2006.

[77] S. J. Lim, S.-j. Kwon, H. Kim, and J.-S. Park, "High performance thin film transistor with low temperature atomic layer deposition nitrogen-doped ZnO," *Applied Physics Letters,* vol. 91, p. 183517, 2007.

[78] O. Erturk, E. Battal, S. E. Kucuk, A. K. Okyay, and T. Akin, "A plasmonically enhanced pixel structure for uncooled microbolometer detectors," 2013, pp. 87041E-87041E-7.

[79] Y. J. Liu, Y. B. Zheng, J. Liou, I. K. Chiang, I. C. Khoo, and T. J. Huang, "All-Optical Modulation of Localized Surface Plasmon Coupling in a Hybrid System Composed of Photoswitchable Gratings and Au Nanodisk Arrays," *The Journal of Physical Chemistry C,* vol. 115, pp. 7717-7722, 2011/04/21 2011.

[80] Z. Zheng, G. Yang, H. Li, and X. Liu, "Three-stage Fabry–Perot liquid crystal tunable filter with extended spectral range," *Optics Express,* vol. 19, pp. 2158-2164, 2011/01/31 2011.

[81] D. Sridharan, R. Bose, H. Kim, G. S. Solomon, and E. Waks, "A reversibly tunable photonic crystal nanocavity laser using photochromic thin film," *Optics Express,* vol. 19, pp. 5551-5558, 2011/03/14 2011.

[82] P. Dong, S. Liao, H. Liang, R. Shafiiha, D. Feng, G. Li, X. Zheng, A. V. Krishnamoorthy, and M. Asghari, "Submilliwatt, ultrafast and broadband electro-optic silicon switches," *Optics Express,* vol. 18, pp. 25225-25231, 2010/11/22 2010.

[83] J. r. B. Kinzel, D. Rudolph, M. Bichler, G. Abstreiter, J. J. Finley, G. Koblmüller, A. Wixforth, and H. J. Krenner, "Directional and Dynamic Modulation of the Optical Emission of an Individual GaAs Nanowire Using

Surface Acoustic Waves," *Nano Letters,* vol. 11, pp. 1512-1517, 2011/04/13 2011.
[84] R. Takigawa, E. Higurashi, T. Suga, and T. Kawanishi, "Air-gap structure between integrated LiNbO3 optical modulators and micromachined Si substrates," *Optics Express,* vol. 19, pp. 15739-15749, 2011/08/15 2011.
[85] I. Moreno, J. A. Davis, T. M. Hernandez, D. M. Cottrell, and D. Sand, "Complete polarization control of light from a liquid crystal spatial light modulator," *Optics Express,* vol. 20, pp. 364-376, 2012/01/02 2012.
[86] M. A. Jacobson, O. V. Konstantinov, D. K. Nelson, S. O. Romanovskii, and Z. Hatzopoulos, "Absorption spectra of GaN: film characterization by Urbach spectral tail and the effect of electric field," *Journal of Crystal Growth,* vol. 230, pp. 459-461, 2001.
[87] V. Alex, S. Finkbeiner, and J. Weber, "Temperature dependence of the indirect energy gap in crystalline silicon," *Journal of Applied Physics,* vol. 79, pp. 6943-6946, 1996.
[88] W. Naoki, K. Tsunenobu, and S. Jun, "Thermo-Optic Coefficients of 4H-SiC, GaN, and AlN for Ultraviolet to Infrared Regions up to 500 °C," *Japanese Journal of Applied Physics,* vol. 51, p. 112101, 2012.
[89] S. J. Lim, S. Kwon, and H. Kim, "ZnO thin films prepared by atomic layer deposition and rf sputtering as an active layer for thin film transistor," *Thin Solid Films,* vol. 516, pp. 1523-1528, 2008.
[90] M.-J. Lee, C. B. Lee, D. Lee, S. R. Lee, M. Chang, J. H. Hur, Y.-B. Kim, C.-J. Kim, D. H. Seo, S. Seo, U. I. Chung, I.-K. Yoo, and K. Kim, "A fast, high-endurance and scalable non-volatile memory device made from asymmetric Ta2O5−x/TaO2−x bilayer structures," *Nat Mater,* vol. 10, pp. 625-630, 2011.
[91] H. Akinaga and H. Shima, "Resistive random access memory (ReRAM) based on metal oxides," *Proceedings of the IEEE,* vol. 98, pp. 2237-2251, 2010.
[92] S. H. Jo and W. Lu, "CMOS compatible nanoscale nonvolatile resistance switching memory," *Nano Letters,* vol. 8, pp. 392-397, 2008/02/01 2008.
[93] S. Yu, H.-Y. Chen, B. Gao, J. Kang, and H. S. P. Wong, "HfOx-based vertical resistive switching random access memory suitable for bit-cost-effective three-dimensional cross-point architecture," *ACS Nano,* vol. 7, pp. 2320-2325, 2013/03/26 2013.
[94] B. Choi, J. J. Yang, M. X. Zhang, K. Norris, D. A. Ohlberg, N. Kobayashi, G. Medeiros-Ribeiro, and R. S. Williams, "Nitride memristors," *Applied Physics A,* vol. 109, pp. 1-4, 2012/10/01 2012.
[95] A. Geresdi, M. Csontos, A. Gubicza, A. Halbritter, and G. Mihaly, "A fast operation of nanometer-scale metallic memristors: highly transparent conductance channels in Ag2S devices," *Nanoscale,* vol. 6, pp. 2613-2617, 2014.
[96] B. F. Bory, H. L. Gomes, R. A. J. Janssen, D. M. de Leeuw, and S. C. J. Meskers, "Role of hole injection in electroforming of LiF-polymer memory diodes," *The Journal of Physical Chemistry C,* vol. 116, pp. 12443-12447, 2012/06/14 2012.
[97] L. Wootae, P. Jubong, S. Myungwoo, L. Joonmyoung, J. Seungjae, K. Seonghyun, P. Sangsu, S. Jungho, and H. Hyunsang, "Excellent state stability of Cu/SiC/Pt programmable metallization cells for nonvolatile memory applications," *Electron Device Letters, IEEE,* vol. 32, pp. 680-682, 2011.
[98] S. Balasubramanian, V. Kumar, N. Balasubramanian, and V. Premachandran, "Resistance switching in indium phosphide using hydrogen passivation of acceptors," *Applied Physics Letters,* vol. 64, pp. 2256-2257, 1994.

[99] R. Waser and M. Aono, "Nanoionics-based resistive switching memories," *Nat Mater,* vol. 6, pp. 833-840, 2007.
[100] R. Waser, R. Dittmann, G. Staikov, and K. Szot, "Redox-based resistive switching memories – nanoionic mechanisms, prospects, and challenges," *Advanced Materials,* vol. 21, pp. 2632-2663, 2009.
[101] U. Russo, D. Ielmini, C. Cagli, and A. L. Lacaita, "Self-accelerated thermal dissolution model for reset programming in unipolar resistive-switching memory (RRAM) devices," *Electron Devices, IEEE Transactions on,* vol. 56, pp. 193-200, 2009.
[102] R. Yang, K. Terabe, G. Liu, T. Tsuruoka, T. Hasegawa, J. K. Gimzewski, and M. Aono, "On-demand nanodevice with electrical and neuromorphic multifunction realized by local ion migration," *ACS Nano,* vol. 6, pp. 9515-9521, 2012/11/27 2012.
[103] D.-H. Kwon, K. M. Kim, J. H. Jang, J. M. Jeon, M. H. Lee, G. H. Kim, X.-S. Li, G.-S. Park, B. Lee, S. Han, M. Kim, and C. S. Hwang, "Atomic structure of conducting nanofilaments in TiO2 resistive switching memory," *Nat Nano,* vol. 5, pp. 148-153, 2010.
[104] K. M. Kim, B. J. Choi, Y. C. Shin, S. Choi, and C. S. Hwang, "Anode-interface localized filamentary mechanism in resistive switching of TiO2 thin films," *Applied Physics Letters,* vol. 91, pp. -, 2007.
[105] K. Hoffmann and D. Hahn, "Electron spin resonance of lattice defects in zinc oxide," *physica status solidi (a),* vol. 24, pp. 637-648, 1974.
[106] A. Pöppl and G. Völkel, "ESR and photo-ESR investigations of zinc vacancies and interstitial oxygen ions in undoped ZnO ceramics," *physica status solidi (a),* vol. 125, pp. 571-581, 1991.
[107] C. A. Wolden, T. M. Barnes, J. B. Baxter, and E. S. Aydil, "Infrared detection of hydrogen-generated free carriers in polycrystalline ZnO thin films," *Journal of Applied Physics,* vol. 97, pp. -, 2005.
[108] S. Basu, B. J. Lee, and Z. M. Zhang, "Infrared radiative properties of heavily doped silicon at room temperature," *Journal of Heat Transfer,* vol. 132, pp. 023301-023301, 2009.